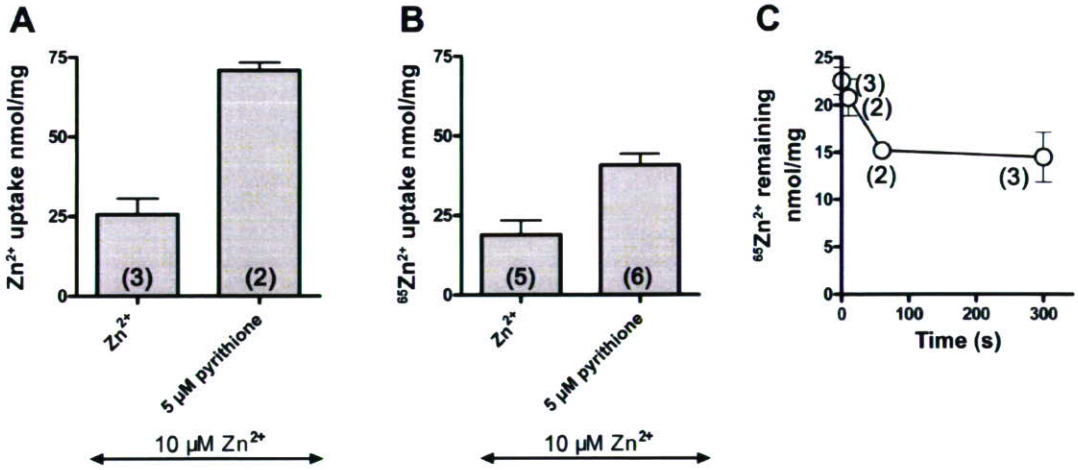

Fig. 2. Cortical neurons, attached to coverslips, were treated with various conditions, as described below, for 30 min, then rinsed 3× with loCa Locke's buffer containing 100 μM EDTA, lysed by freezing at −80°C, scraped, and resuspended for Zn^{2+} analysis by inductively coupled plasma-mass spectrometry (ICP-MS; *A*) or treated as in *A* with the addition of $^{65}Zn^{2+}$ (*B*), and lysate radioactivity was determined by liquid scintillation counting. Lysate protein was determined by Bio-Rad protein assay using BSA as a standard. Each bar represents mean ± SE; nos. in parentheses are the no. of replicates. An unpaired *t*-test showed that, for either *A* or *B*, Zn^{2+} uptake after pyrithione treatment was significantly increased ($P < 0.01$). *C*: cortical neurons attached to glass coverslips were removed from neurobasal (NB) media to loCa Locke's buffer for 1 min at 37°C. Coverslips were then treated for 30 min with 10 μM Zn^{2+} containing $^{65}Zn^{2+}$. Coverslips were moved to loCa Locke's buffer containing 100 μM EDTA for various times, then briefly rinsed 3× in fresh loCa Locke's buffer/100 μM EDTA, and treated as described for *B*. Data are presented as means ± SE; nos. in parentheses are the no. of replicates.

some ZnAF-2F was Zn^{2+} bound (as evidenced by the effects of TPEN addition). Resting levels of ZnAF-2F saturation with Zn^{2+} varied when measured in individual coverslips (16.3 ± 1.2%, mean ± SE, $n = 10$), and usually ranged between 10 and 20%.

We observed a steady increase in ZnAF-2F fluorescence when neurons were placed in buffer with added Zn^{2+} (i.e., Zn^{2+} influx, Fig. 3*A*). We found that the $\Delta F/F_0$ was dependent on extracellular Zn^{2+} concentration, as would be expected for transporter mediated Zn^{2+} uptake. The $\Delta F/F_0$ ($\Delta F/F_0$ per second) was computed from linear regression analysis of the first minute of data collected. These rates were then plotted as a function of extracellular Zn^{2+} concentration and fit to a rectangular hyperbola to obtain K_m for transporter-mediated Zn^{2+} influx ($K_m = 4.65$ μM). This K_m value is consistent with previous kinetic measurements of Zn^{2+} transport mediated by SLC39A1 (23) in cultured cells. With the addition of pyrithione, ZnAF-2F fluorescence rapidly reached a maximum (additional increases in Zn^{2+} concentration did not increase fluorescence, data not shown). After TPEN addition, a new steady state in intracellular free Zn^{2+} was obtained, yielding a fluorescence slightly less than at the start of the reaction, identical to that obtained without addition of Zn^{2+} (Fig. 3*A*). In Fig. 3*B*, the experimental data are reported as percent saturation to allow direct comparison with model results. It can be seen in Fig. 3*B* that, after 3-min exposure to 30 μM Zn^{2+}, ZnAF-2F was ~40% saturated.

Constraints used for model development. Parameter values for fluorophore binding are known. Transport K_m and V_{max} were fixed from the experiments described above. Other parameter values were constrained by experimental results. Key experimental constrains reported above are as follows: *1*) fluorescence at rest is 16% of maximum, on average; *2*) total neuronal Zn^{2+} content is 250 μM at rest; *3*) total Zn^{2+} content rises by an additional 320 μM when the cell is exposed to 10 μM extracellular Zn^{2+} for 30 min and reaches a maximum capacity of 1.5 mM when pyrithione is also present; *4*) the percent saturation of the fluorophore rises from 16% at rest to 39% after 3-min exposure to 30 μM extracellular Zn^{2+}; *5*) the $\Delta F/F_0$ upon exposure to 30 μM extracellular Zn^{2+} is linear for 3 min, increases steeply, and saturates following pyrithione application and decays upon exposure to TPEN, as shown in Fig. 3. These constraints determine the resting bound and unbound concentrations of ZnAF-2F and constrain parameter value choices for the size and kinetics of the muffler in our three models.

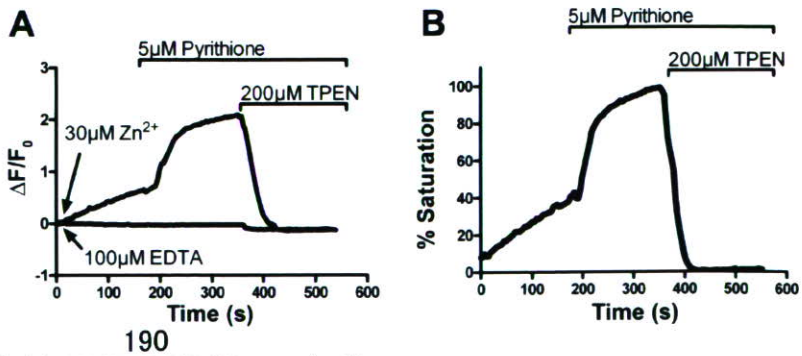

Fig. 3. *A*: cortical neurons loaded with 5 μM ZnAF-2F were treated with either 100 μM EDTA or 30 μM Zn^{2+}; 5 μM pyrithione at 3 min and 200 μM TPEN at 6 min were added to loCa Locke's buffer. *B*: raw data from *A* with 30 μM Zn^{2+} added, expressed as percent saturation (see MATERIALS AND METHODS). $\Delta F/F_0$, rate of fluorescence increase.

The buffer model (model 1) cannot explain the experimental results. In the buffer model, there are only three unknown parameter values (total buffer concentration, on and off rates for Zn^{2+} binding to buffer), and the experimental constraints should be sufficient to allow all parameter values to be determined uniquely. However, no set of parameter values satisfied all of the constraints. Resting total Zn^{2+} level and Zn^{2+} capacity required a buffer with a K_d of 5.1 nM. Slow buffer on and off binding rate constants could match the 3-min fluorescence value, but the increase in fluorescence was very hyperbolic; fast buffer rate constants made the increase in fluorescence linear, but the 3-min fluorescence value was much too small (Fig. 4*A*). No set of rate constants could match both the linearity of the fluorescence increase and the value at 3 min found experimentally.

We then dropped the constraint that resting total Zn^{2+} was 250 μM, assuming that perhaps the *model 1* reactions occur independently of a large unreactive pool of Zn^{2+} [e.g., the nucleosome (1)]. In this case, buffer K_d was 78 nM to match the total Zn^{2+} capacity and the 3-min fluorescence value (solid line in Fig. 4*A*; parameter values given in Tables 1 and 2). However, the model still did not match the experimental data very well. The fluorescence increase predicted by the model was never linear, typically having an initial delay and a later hyperbolic bend. Even more noticeable were the poor fits to the experimental data when pyrithione and TPEN were added. The fluorescence increase predicted by the model when pyrithione was added was far too small, unless the value for k_{pyr} was increased, but when k_{pyr} was increased, the fit after TPEN addition was poor (Fig. 4*B*). Finally, we note that there are a number of substances that bind Zn^{2+} with micromolar affinity, or an affinity much weaker than the 78 nM found here [e.g., glutathione (40)]. While a buffer with a 10-fold lower affinity can match the 3-min fluorescence value, this happens in the model only for a total Zn^{2+} capacity nearly 10-fold larger, in contradiction to the experimental constraint.

Insights and predictions from the muffler model (model 2). The muffler model (*model 2*) has seven free parameters: buffer (muffler) concentration, deep-store Zn^{2+} concentration, on and off muffler Zn^{2+} binding rates, on and off rates to the deep store, and leak from the deep store. While the experimental data could not fix all of the parameter values uniquely for this

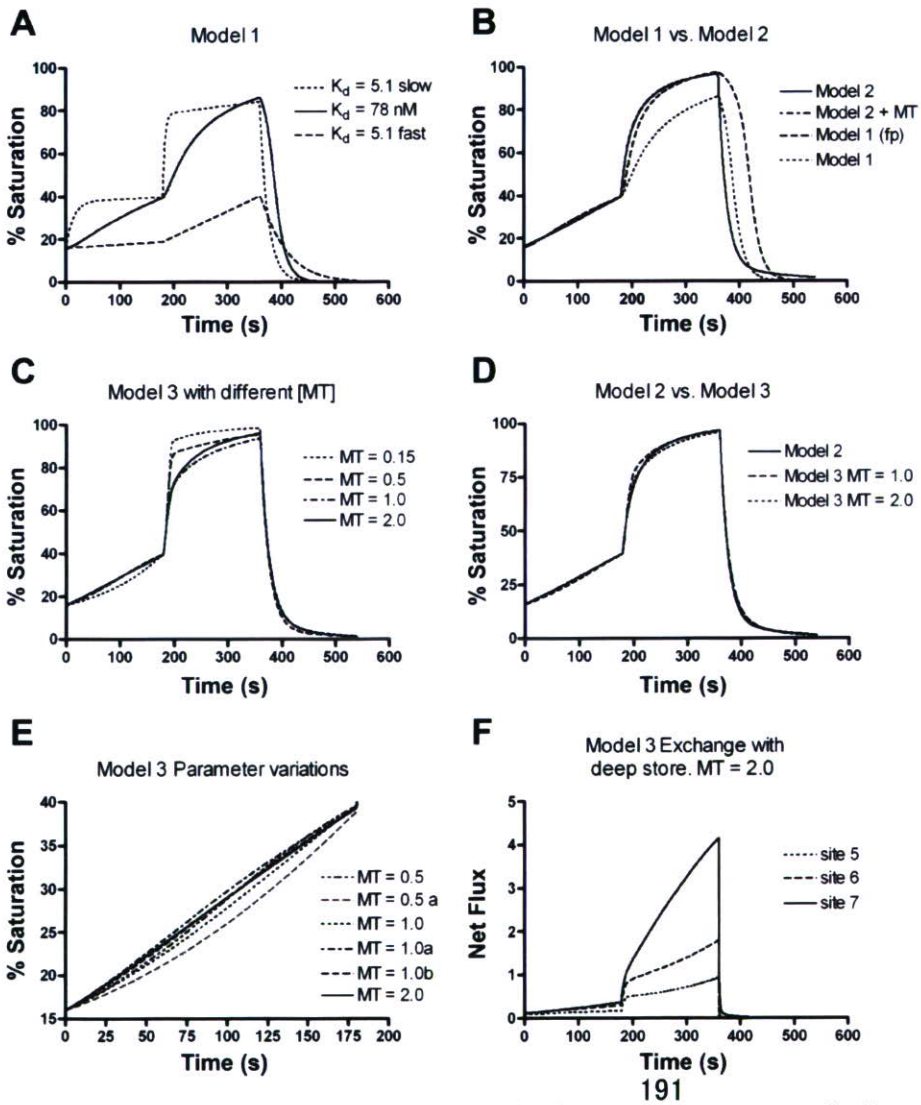

Fig. 4. Comparison of predictions using *models 1*, *2*, and *3*. In all cases, extracellular Zn^{2+} is 30 μM, pyrithione is applied at 3 min, and TPEN at 6 min (see Fig. 3*B*). Parameter values are given in Tables 1 and 2, except as noted below. *A*: *model 1* results, with and without the constraint that total resting Zn^{2+} is 250 μM. With the constraint, buffer K_d is 5.1 nM, and starting S and SZn_i values are 1,216 and 249.28 μM, respectively. Results are shown when buffer rate constants (k_{b1}, k_{b2}) are either fast (dashed line; 10, 0.05122) or slow (dotted line; 0.08, 0.00041). Without the constraint, buffer K_d is 78 nM (solid line); parameter values are those for *model 1* in Tables 1 and 2. *B*: *model 2* predictions with and without metallothionein (MT) added (curves overlap) compared with *model 1* results (buffer K_d = 78 nM) with k_{pyr} = 0.052 or 0.15 [fast pyrithione rate (fp)]. *C*: MT as the exclusive muffler (*model 3*). Predictions are shown for MT concentrations of 0.15, 0.5, 1.0, and 2.0 μM. *D*: comparison of *model 2* predictions with *model 3* results for MT = 1.0 and 2.0 μM. *E*: a blow-up of the first 180 s showing the lack of linearity with various parameter value choices when MT = 0.5 or 1.0 μM compared with the MT = 2.0 μM case. Parameter values are as in Tables 1 and 2 for MT = 0.5, 1.0, and 2.0 μM cases. For cases labeled MT = 0.5a, MT = 1.0a, and MT = 1.0b, parameter values (k_{b2}, k_{r52}, k_{r62}, k_{r72}, k_1) were 0.012, 0.005, 0.002, $1e^{-6}$, 0.0037; 0.009, 0.025, 0.01, $5e^{-6}$, 0.015; and 0.008, 0.005, 0.002, $1e^{-6}$, 0.015, respectively. In addition, k_{r51}, k_{r61}, and k_{r71} were 3, 3, and 3, respectively, for the MT = 0.5a case. Starting concentration values, similar to those in Table 2, were recomputed with these rate constant changes. *F*: net flux to the deep store from MT Zn^{2+} binding *sites 5* (K_d = 40 pM), *6* (K_d = 100 pM), and *7* (K_d = 20 nM). *Model 3* with MT = 2 μM.

model, the data severely constrained parameter value choices, and sets of parameter values that satisfied all of the experimental constraints shared important features in common. First, the muffler had to have a high affinity for Zn^{2+} with a fast on-rate constant for Zn^{2+} binding. Good solutions were found with K_d values of 60–80 pM with on-rate constants of $80–100 \times 10^{-6}$ $M^{-1} \cdot s^{-1}$. Lower affinity and slower on-rate constants introduced an early bump in the fluorescence increase, and higher affinity values produced a bowed curve, unlike the experimental data, which showed a linear increase in fluorescence in the initial 3 min of exposure to 30 μM of extracellular Zn^{2+} (Fig. 3*B*). Because of its high affinity, 210–240 μM of the 250 μM total Zn^{2+} in the cell at rest was bound to this muffler. Second, free muffler concentration was consistently between 15–25 μM for good solutions. This is a consequence of the choice of the K_d value for Zn^{2+} binding to the muffler. If the muffler K_d was greater than 120 pM, the amount of free muffler in the model had to be very high; ZnAF-2F fluorescence upon exposure to 30 μM extracellular Zn^{2+} then rose much more slowly than in the experiments, because Zn^{2+} would bind to the free muffler rather than to ZnAF-2F. Small muffler K_d values produced the opposite problem; the amount of free muffler was small and it became quickly overwhelmed when Zn^{2+} influx was increased. The rate constants for muffler interaction with the deep store could be tuned to compensate somewhat for these problems, but this introduced other problems with the solutions, such as bowing or an early bump in the fluorescence curve mentioned earlier. Third, the resting amount of Zn^{2+} in the deep store was 12–30 μM with parameter value choices that produced results matching the data. This forms a prediction of the amount of Zn^{2+} in mitochondria, Golgi, and other organelles at rest.

The muffler model results given so far assume that the 250 μM total Zn^{2+} in the neuron is all available for the reactions modeled, but, as mentioned above, it is possible that a significant portion of cellular Zn^{2+} may be so tightly bound or otherwise shielded, even from a muffler with a K_d of 60–80 pM, to make it unavailable to the model reactions (1). Thus simulations were done assuming that only 100 μM of the total Zn^{2+} were available to the model reactions. The major difference from the previous results was that the K_d of Zn^{2+} binding to the muffler that provided the best fits was larger (80–300 pM). For good solutions, the on-rate for Zn^{2+} binding still had to be large, and free muffler concentration and resting deep-store Zn^{2+} concentration were in the same ranges as before (12–27 and 14–30 μM, respectively).

Incorporating MT into the model (models 2 and 3). Because of the significant role MT is thought to play in Zn^{2+} homeostasis (37), we added MT as a Zn^{2+} buffer to the muffler model (*model 2*) to see what effect this would have on the results. We chose a concentration of 1 μM, yielding 7 μM of Zn^{2+} binding sites. This concentration is in excess of the 0.34 μM actually determined, to allow an effect to be seen more clearly, if there is one. Total muffler concentration had to be reduced by ~7 μM to continue to satisfy the experimental constraints, but the overall effect on the results was negligible (curves entirely overlap in Fig. 4*B*). At rest, MT Zn^{2+} binding *sites 1-6* were nearly saturated, and *site 7* was largely free, and there was little change during exposure to 30 μM extracellular Zn^{2+} for 3 min, aside from a low level of Zn^{2+} binding to *site 7*.

Given this result, we turned to a third model, the MT as muffler model (*model 3*). In this model, the muffler of *model 2* became a simple buffer (additional buffer capacity must be included to bind the 250 μM total resting Zn^{2+} in the neuron), and MT was postulated as the exclusive route for trafficking Zn^{2+} to the deep store. Results computed with different values for MT concentration are shown in Fig. 4*C*. There were a number of interesting features uncovered with these models. First, the results with *model 3* approached those of *model 2* (and also the experimental results) only for the largest values of MT concentration tested (Fig. 4*D*). Models with 0.15, 0.5, and even 1.0 μM of MT had trouble producing a linear increase in fluorescence over the first 3 min, as seen experimentally. Curves would bow, bend, or assume a sigmoid appearance, depending on the particular parameter values chosen (Fig. 4*E*). Such variations were particularly sensitive to buffer affinity. The reason for these deviations from linearity was that low MT concentrations were not sufficient to transfer Zn^{2+} to the deep store fast enough, forcing the buffer (and the fluorophore) to handle an increasing amount of the Zn^{2+} load. Making the transfer reaction arbitrarily fast in the model did not help, because the leak rate constant had to be increased as well because of the Zn^{2+} capacity constraint (see MATERIALS AND METHODS). In contrast, if MT concentration was 2.0 μM, the amount of Zn^{2+} that could be shuttled to the deep store in 3 min approached that in the muffler model (*model 2*), and linearity in the fluorescence increase was more easily obtained. Second, as can be seen with the parameter values in Table 2, Zn^{2+} binding *sites 5* and *6* on MT are not saturated at rest in this model as they were when MT was a simple Zn^{2+} buffer. In fact, these sites range from being half saturated to being largely free of Zn^{2+} in these models (see Table 2; Fig. 4*E* legend); this is a result of the muffling reaction between these sites and the deep store. Third, even though *site 7* has a lower affinity for Zn^{2+} than *sites 5* and *6* and is always largely free of Zn^{2+} at rest, it turns out that the net Zn^{2+} flux to the deep store is greater from *site 7* than from *site 6* after the first minute, and both *sites 6* and *7* had greater Zn^{2+} flux to the deep store than *site 5* (Fig. 4*F*). This may be a consequence of our choice of rate constants (Table 1) that were based on the assumption that rates for the interaction of a Zn^{2+}-bound MT Zn^{2+} binding site with the deep store should be related to the affinity of the individual binding sites for Zn^{2+}. Also, as might be expected, net fluxes were much smaller when MT concentration was 0.15, 0.5, or 1.0 μM. Finally, we note that results were sensitive to the value of the on-binding rate of Zn^{2+} to MT relative to the Zn^{2+} on-binding rate to the buffer, perhaps reflecting competition for Zn^{2+}, because the K_d of the buffer was similar to that of MT Zn^{2+} binding *sites 5* and *6* (data not shown). Because the muffler model (*model 2*) is the best constrained model and it matches the experimental data well, we use this model for all further model predictions and comparisons to experimental data.

The intracellular free Zn^{2+} concentration. While the models assumed that the fluorophore was 16% saturated at rest, there was variation in this percentage among individual experiments. The muffler model was used to explore the consequences of these differences. An important experimental constraint for these simulations was that the slope of the fluorescence increase during the first 3 min was independent of the starting saturation percentage. Parameter values were found that satis-

fied the constraint that the total resting Zn^{2+} content is 250 μM for all starting saturation percentages, but the use of these values caused the slopes of the fluorescence increases to be different, in contradiction to the experimental data. To match the slopes found in the data, we let total Zn^{2+} content vary, and results are shown in Fig. 5*A*. The starting saturation percentage not only determined the intracellular free Zn^{2+} concentration as expected, but it also determined the total Zn^{2+} in the neuron, the total muffler concentration, and the total Zn^{2+} capacity. For example, if we compare starting saturation percentages of 8 and 20%, the resting intracellular free Zn^{2+} concentration is 0.5 and 1.4 nM, total resting Zn^{2+} content is 146 and 277 μM, total muffler concentration is 163 and 272 μM, free muffler concentration is 24.3 and 16.1 μM, and total Zn^{2+} capacity is 1 and 1.6 mM, respectively. The intracellular free Zn^{2+} concentration is maintained in a narrow range by comparatively large changes in total muffler concentration (which determines resting Zn^{2+} content and capacity), whereas free muffler concentration remains in a much more narrow range.

Next, the muffler model was used to predict how much the presence of ZnAF-2F (i.e., the Zn^{2+} buffering effect of ZnAF-2F itself) distorted the intracellular free Zn^{2+} concentration. The distortion was small, as shown in Fig. 5, *B* and *C*. Using *model 2* (16% ZnAF-2F saturation at rest), the concentration of ZnAF-2F bound with Zn^{2+} was 758 nM. When ZnAF-2F was removed from the model and this 758 nM was added to the free Zn^{2+} concentration, the system reached a new equilibrium in which ~47% of the 758 nM went to the deep store and 53% became bound to free muffler. The result was a 26 pM increase in the resting free Zn^{2+} concentration. Upon exposure to 30 μM extracellular Zn^{2+} for 3 min, the difference in free Zn^{2+} concentration with and without ZnAF-2F was 183 pM (Fig. 5*C*). Subsequent application of pyrithione increased free Zn^{2+} levels, but the difference with and without ZnAF-2F was only 4.5 nM at the peak (Fig. 5*B*). Thus the model predicts that cultured neurons have an intrinsic Zn^{2+} buffer capacity far in excess of that potentially added by 5 μM ZnAF-2F. The cytosolic buffer (working in concert with a deep store) is able to "absorb" nearly all of the Zn^{2+} that enters the neuron when Zn^{2+} influx is increased.

The Zn^{2+} buffer capacity of cultured cortical neurons, therefore, might be expected to be greater than that of HT-29 cells, which have been studied by Krezel and Maret (38). The presumed large buffer capacity of neurons should allow for the application of the equation (25):

$$[Zn^{2+}] = K_d\left(\frac{F - F_{min}}{F_{max} - F}\right) \quad (2)$$

to calculate the intracellular free Zn^{2+} concentration with reasonable accuracy (see Fig. 5, *B* and *C*). It can be seen that model predictions of intracellular free Zn^{2+} concentration changes and those calculated using the above equation agree quite well when ZnAF-2F is only partially saturated. As ZnAF-2F nears 100% saturation, the equation tends to significantly overestimate free Zn^{2+} concentration (Fig. 5*D*). This is largely because F_{max} estimated as addition of Zn^{2+} and pyrithione probably slightly underestimates the true F_{max}. This inaccuracy in estimating F_{max} becomes exaggerated as F approaches F_{max}, making the denominator in the above equation quite small. In other cell types with a much smaller intrinsic Zn^{2+} buffer capacity, intracellular fluorophores may act as significant competing cytosolic buffers and will "clamp" changes in intracellular free Zn^{2+} concentration (12, 45), such that the intracellular free Zn^{2+} concentration will largely depend on the fluorophore concentration, invalidating the above equation.

A kinetic analysis of Zn^{2+} efflux and model simulations of efflux. Neurons loaded with 5 μM ZnAF-2F were exposed to either 30 μM extracellular Zn^{2+} (Fig. 6*A*), or 30 μM extracel-

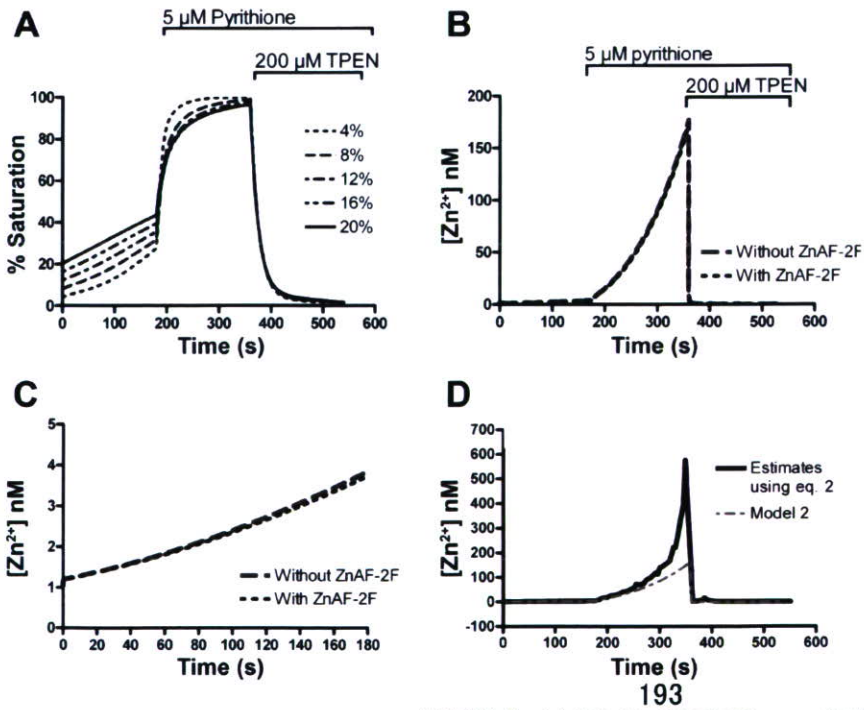

Fig. 5. *A*: starting ZnAF-2F saturation is varied from 4 to 20%. Starting values for Zn^{2+}, free muffler, bound muffler, deep store Zn^{2+}, and total Zn^{2+} are 0.23 nM, 27 μM, 74 μM, 3.4 μM, 78 μM; 0.48 nM, 24.3 μM, 139 μM, 7 μM, 146 μM; 0.75 nM, 21.8 μM, 194 μM, 11 μM, 205 μM; 1.05 nM, 19 μM, 234 μM, 15.2 μM, 250 μM; and 1.4 nM, 16.1 μM, 256 μM, 19.7 μM, 277 μM for 4, 8, 12, 16, and 20% starting saturation levels, respectively. *B* and *C*: using *model 2*, data were derived for changes in intracellular free Zn^{2+} concentration as a function of time, with and without ZnAF-2F present when 30 μM extracellular Zn^{2+} was added. *B*: effects of Zn^{2+} addition followed by pyrithione for 3 min and then TPEN. *C*: changes for the first 3 min only. *D*: *model 2*-derived predictions for changes in intracellular free Zn^{2+} concentration after addition of 30 μM Zn^{2+} are plotted on the same graph as experimentally derived estimates using *Eq. 2*. ZnAF-2F K_d = 5.5 nM, maximum fluorescence (F_{max}) = fluorescence measured after the addition 30 μM Zn^{2+} and pyrithione, and minimum fluorescence (F_{min}) = fluorescence measured after addition of TPEN.

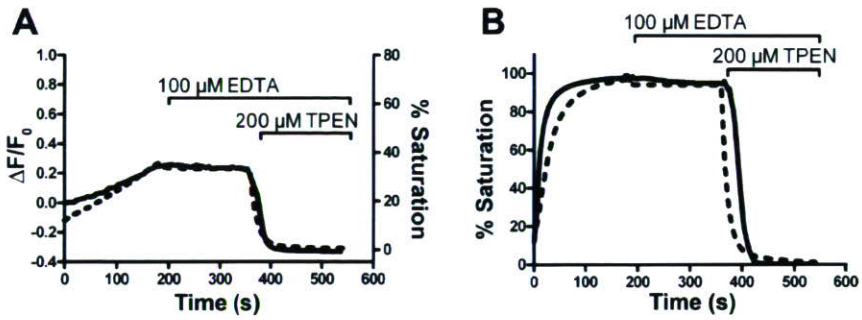

Fig. 6. Experimental data (solid line) and *model 2*-derived predictions (dotted line) plotted together on the same graphs. *A*: experimental data. Cortical neurons were loaded with 5 μM ZnAF-2F and treated with 30 μM Zn^{2+} for 3 min, and then 100 μM EDTA for 3 min, and finally with 200 μM TPEN. Data are expressed as $\Delta F/F_0$ (*left* axis). *B*: experimental data. Cortical neurons were treated with 5 μM pyrithione and 30 μM Zn^{2+} for 3 min, and then as in *A*. Raw data were converted to %saturation (see MATERIALS AND METHODS). *Model 2* predictions (*A* and *B*) are expressed as %saturation and scaled to match the experimental data (*right* axis in *A*). Each experimental plot is the mean of data obtained from 3 individual coverslips.

lular Zn^{2+} and 5 μM pyrithione (Fig. 6*B*). Addition of 30 μM extracellular Zn^{2+} resulted in a roughly linear rise in ZnAF-2F fluorescence (Fig. 6*A*). Addition of pyrithione at the start of a reaction resulted in a much faster rate of Zn^{2+} influx, as shown by the rapid increase in ZnAF-2F fluorescence that quickly reached near saturation levels (Fig. 6*B*). After 3 min, 100 μM EDTA were added to block Zn^{2+} influx, thus allowing for unopposed Zn^{2+} efflux. The time course of the decrease in ZnAF-2F fluorescence after EDTA addition, with or without addition of pyrithione, appeared to follow a slow but steady decline. The observed changes in ZnAF-2F fluorescence were completely and rapidly reversed by the addition of TPEN. These findings are entirely consistent with our contention that the vast majority of newly transported Zn^{2+} (even in the presence of pyrithione) is buffered and intracellular free Zn^{2+} remains in the nanomolar range. The match between *model 2* predictions and the experimental data was quite good (see Fig. 6). The model predicted an initial small but rapid decline followed by a much slower but steady decline after addition of EDTA. The small, rapid decline was caused by the fast redistribution of Zn^{2+} between intracellular ZnAF-2F and the muffler once influx was stopped. This small decline could be converted into a large decline (or even a large increase) in the model by scaling the ZnAF-2F rate constants. The subsequent longer, slower decline reflects Zn^{2+} concentration gradient-dependent Zn^{2+} efflux, modeled as a simple reversal of the influx transporter. It appeared that the experimental data were unable to resolve the small, rapid initial decline in fluorescence from the slow and steady Zn^{2+} efflux. Regardless, both the model and experimental data agree that the intracellular free Zn^{2+} concentration must remain low, even in the face of much larger net Zn^{2+} uptakes and that Zn^{2+} efflux remain small, most likely as a result of the low intracellular free Zn^{2+} levels (i.e., large intrinsic buffering capacity). Thus the plateau in ZnAF-2F fluorescence observed after addition of pyrithione reflects mostly ZnAF-2F saturation.

Addition of CQ and Zn^{2+} resulted in a large increase in Zn^{2+} influx and net uptake of Zn^{2+}. A previous study has suggested that CQ might act as a Zn^{2+} ionophore, but did not directly measure an increase in cellular Zn^{2+} content after CQ addition (13). We made direct measurements of Zn^{2+} uptake in the presence of low micromolar concentrations of CQ to confirm this finding, and we felt we could test the validity of the model by including CQ actions. Figure 7 shows images illustrating the increase in fluorescence observed after neurons were incubated with 30 μM Zn^{2+} or 30 μM Zn^{2+} and 1 μM CQ for 5 min (compare Fig. 7, *A* and *B*). Next, neurons treated with Zn^{2+} and CQ were subsequently treated with 200 μM TPEN, showing that the increase in intracellular fluorescence was completely reversed (Fig. 7*C*). Results of quantifying the changes in cellular fluorescence intensity observed in Fig. 7, *A–C*, are shown in Fig. 7*D*. These findings were confirmed by determination of total cellular Zn^{2+} uptake using ICP-MS analysis and $^{65}Zn^{2+}$ uptake as shown in Fig. 8. No effect of 100 nM CQ upon Zn^{2+} uptake after incubation with 10 μM extracellular Zn^{2+} was observed (Fig. 8, *A* and *B*). When Zn^{2+} and 3 μM CQ were added, both $^{65}Zn^{2+}$ uptake and total cellular Zn^{2+} determined by ICP-MS analysis were increased to levels similar to that seen with the addition of 5 μM pyrithione and Zn^{2+} (compare Figs. 2 and 8). The effects of CQ on the cellular Zn^{2+} content were specific, as no change in total Mn, Fe, or Cu levels were observed by ICP-MS analysis. As shown previously in Fig. 2*C*, exposure of cortical neurons to increased extracellular Zn^{2+} resulted in increased Zn^{2+} surface binding. It was determined also whether addition of CQ resulted in an additional increase in surface binding of Zn^{2+}. As shown in Fig. 8*C*, a small increase in Zn^{2+} surface binding was observed in the presence of CQ, as might be expected for Zn^{2+}/CQ complexes associated with the plasma membrane. However, data presented in Figs. 7 and 8 clearly show that exposure to CQ in the presence of extracellular Zn^{2+} results in an increased intracellular free Zn^{2+} concentration and total Zn^{2+} content.

To incorporate CQ effects into the model, the kinetics of CQ actions on intracellular free Zn^{2+} needed to be determined and were studied using intracellular ZnAF-2F fluorescence changes. No effect of 1 μM CQ was observed after elimination of Zn^{2+} influx by addition of 100 μM EDTA (data not shown). ZnAF-2F fluorescence only decreased slightly to a new steady state, identical to that seen in Fig. 3*A* without CQ addition. Thus the increase in intracellular fluorescence seen in the presence of increased extracellular Zn^{2+} with the addition of CQ was Zn^{2+} dependent and most likely due to increased influx of Zn^{2+}. In addition, if CQ crosses the plasma membrane and enters neurons, as it is likely to do since it is extremely lipophilic, it has no apparent direct action to affect the resting intracellular free Zn^{2+} concentration, either by altering cytosolic Zn^{2+} buffering or causing enough Zn^{2+}

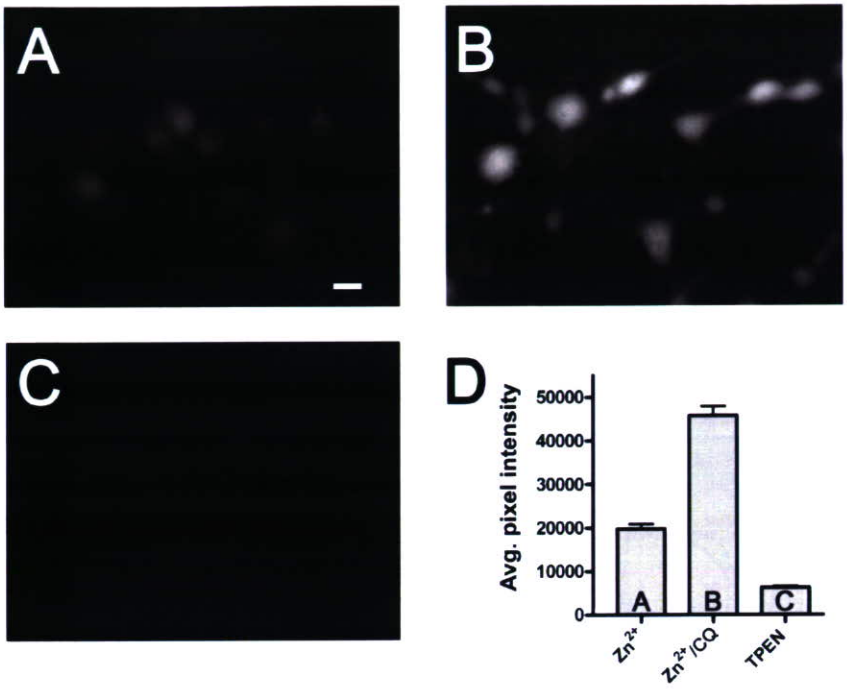

Fig. 7. Cortical neurons attached to glass coverslips were treated as described in Fig. 1 and exposed to 30 μM Zn^{2+} (*A*), or 30 μM Zn^{2+} plus 1 μM CQ (*B*), or same as in *B* followed by 200 μM TPEN (*C*). Cell bodies were analyzed for average pixel intensity, and those data are shown in *D*. Each bar represents mean ± SE (n = 7 individual cells on one coverslip as pictured in *A*–*C*). A Tukey multiple-comparison test (GraphPad Prism, version 4.03) showed that, for any column pair, $P < 0.001$. Size bar = 10 μm.

release from sites of protein binding or organellar sequestration to have an effect on ZnAF-2F fluorescence.

When increasing concentrations of CQ (0.1–3 μM) were added in the presence of 30 μM extracellular Zn^{2+}, the $\Delta F/F_0$ (i.e., Zn^{2+} influx) increased in a concentration-dependent manner (Fig. 9). Addition of pyrithione 3 min after the start of each reaction resulted in a rapid increase in ZnAF-2F fluorescence that quickly reached saturation (see also Fig. 3). At 3 μM CQ, ZnAF-2F was already saturated before pyrithione addition (Fig. 9*D*). Addition of TPEN after pyrithione addition resulted in a complete reversal of the fluorescence signal (Fig. 9). In Fig. 9, results are shown also from the model predictions with CQ added. CQ was modeled as an ionophore, and the responses to 30 μM extracellular Zn^{2+} with the addition of various concentrations of CQ generally followed the experimental data. The primary difference was that the model did not match exactly the dose-dependent increases in Zn^{2+} influx seen experimentally as a result of CQ addition.

Once newly transported Zn^{2+} is sequestered, it cannot be released by CQ. To show if the sequestration of newly transported Zn^{2+} could be disrupted by CQ, CQ was added 3 min after Zn^{2+} influx had been increased by increasing extracellular Zn^{2+} to 30 μM (Fig. 10*A*). At the 3-min reaction time point, either 1 μM CQ or 1 μM CQ and 100 μM EDTA (which will

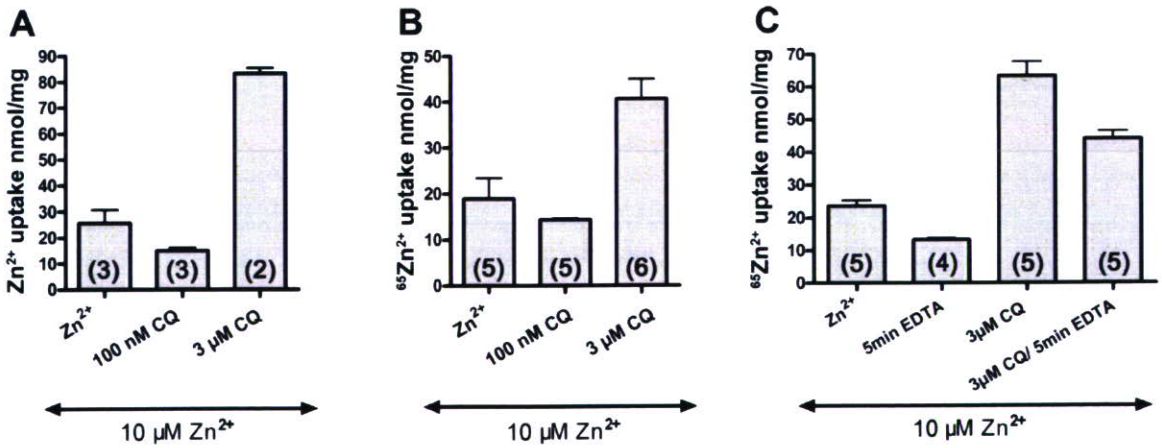

Fig. 8. Cortical neurons were exposed to 10 μM Zn^{2+} with 0, 100 nM, or 3 μM CQ for 30 min, as described in Fig. 2. Results are of ICP-MS analysis (*A*) or treated as in *A* with the addition of $^{65}Zn^{2+}$ and lysate radioactivity determined by liquid scintillation counting (*B*). *C*: cortical neurons treated as in *B*, with or without addition of 100 μM EDTA for 5 min after the 30-min incubation with $^{65}Zn^{2+}$. Lysate protein was determined by Bio-Rad protein assay using BSA as a standard. Each bar represents mean ± SE; nos. in parentheses are the no. of replicates. A Tukey multiple-comparison test (GraphPad Prism, version 4.03) was performed on each data set (*A*, *B*, or *C*) and showed that only the differences between Zn^{2+} and Zn^{2+} with 100 nM CQ (*A* or *B*) and Zn^{2+} and Zn^{2+} with 5-min EDTA treatment (*C*) were not significant; otherwise, all other comparisons were significant ($P \leq 0.01$).

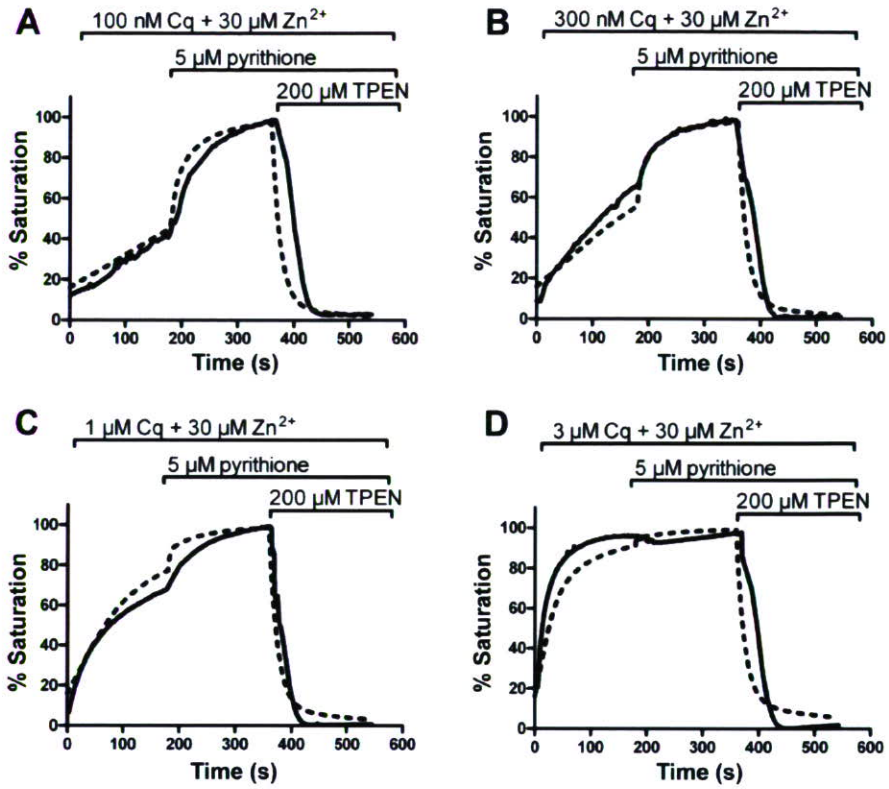

Fig. 9. Experimental data (solid line) and *model 2* predictions (dotted line) plotted together on the same graphs. Cortical neurons were loaded with 5 μM ZnAF-2F and treated with 30 μM Zn^{2+} for 3 min (*A*) with the addition of 100 nM (*A*), 300 nM (*B*), 1 μM (*C*), or 3 μM (*D*) CQ, followed by 5 μM pyrithione for 3 min, and finally 200 μM TPEN. Each plot is the mean of data obtained from 3 individual coverslips.

effectively stop any additional Zn^{2+} influx from that point on) was added. It can be seen that addition of CQ alone resulted in an immediate increase in the $\Delta F/F_0$. Furthermore, this change in the $\Delta F/F_0$ was not observed when Zn^{2+} influx was blocked by the addition of 100 μM EDTA. The results suggest that, once newly transported Zn^{2+} is sequestered intracellularly, it is protected from any action of CQ. These data are consistent also with the idea that CQ affects the transfer of Zn^{2+} across the plasma membrane and does not affect intracellular Zn^{2+} buffering. *Model 2* simulations were done to mimic the experimental conditions of the addition of CQ after Zn^{2+} uptake was initiated, with or without the addition of EDTA. The difference the addition of CQ makes when it is added together with EDTA is shown in Fig. 10*B*, where CQ slightly increases efflux. These data show that the mechanism of action of CQ cannot be explained by a decrease in the rate of efflux, because efflux is low and only increases after the addition of CQ. The *model 2* results match experimental data and, therefore, support the theory that, because of the lipophilic nature of CQ, added CQ is partitioned into cell membranes, and its actions on the intracellular free Zn^{2+} concentration and total Zn^{2+} content are mediated through an ionophoretic action.

DISCUSSION

Insights concerning the resting neuronal Zn^{2+} metallome, intracellular free Zn^{2+}, and Zn^{2+} buffering capacity. We constructed a series of increasingly complex computational models describing Zn^{2+} buffering in the soma of cultured cortical neurons. We found first that the experimental data

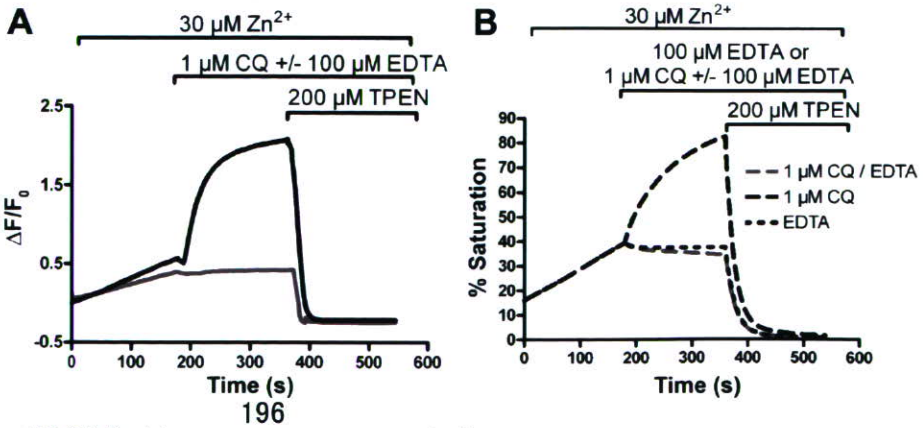

Fig. 10. *A*: cortical neurons were loaded with 5 μM ZnAF-2F and treated with 30 μM Zn^{2+} for 3 min, then treated with 1 μM CQ, with (shaded line) or without (solid line) 100 μM EDTA, and finally treated with 200 μM TPEN. Each plot is the mean of data obtained from 3 individual coverslips. *B*: *model 2* predictions for the experimental conditions as described in *A* (see legend). Model predictions without CQ but with EDTA are plotted also to allow comparison of efflux rates.

cannot be described adequately with a model containing only a simple buffer (*model 1*), regardless of the affinity or capacity of the buffer. We then developed the muffler model (*model 2*) in which Zn^{2+} binding and sequestration is described as a high-affinity muffler (58) in equilibrium with free Zn^{2+} that can deposit Zn^{2+} into a much larger capacity deep store. This model has seven free parameters whose values are heavily constrained by experimental data from several different types of experiments, whose results are reported here. This model was able to reproduce both qualitatively and quantitatively the changes in intracellular free Zn^{2+} concentration observed after extracellular Zn^{2+} was increased to micromolar levels. In addition, this model was able to reproduce the actions of added CQ as well as the effects of added EDTA, pyrithione, or TPEN. Thus *model 2* provides a simple description that appropriately describes the interactions of the primary cellular constituents contributing to the buffering of intracellular free Zn^{2+} concentration in the soma of cultured cortical neurons. *Model 2* predicts that, at rest, the vast majority of the cellular Zn^{2+} is either protein bound or sequestered in organelles (total Zn^{2+} distribution at rest with ZnAF-2F present: 93.6% muffler, 6.1% deep store, 0.3% fluorophore, free Zn^{2+} << 0.1%). The characteristics of the muffler were not determined experimentally, but the muffler is required for model predictions to match experimental data.

While the free parameters of the muffler model (*model 2*) could not be determined uniquely, sets of parameter values that satisfied the experimental constraints shared important features. The muffler had to have high affinity with K_d of 60–100 pM, and the free muffler concentration had to be near 20 μM, characteristics similar to those noted by Krezel and Maret (38). These characteristics, plus the ability to deposit Zn^{2+} into the deep store, allow the muffler to exert a fine control over intracellular free Zn^{2+} concentration over a wide range of Zn^{2+} loads. The model also predicts that 12–30 μM Zn^{2+} resides in the deep store at rest. When neurons are exposed to Zn^{2+} and pyrithione, the total neuronal Zn^{2+} content can be increased nearly 50-fold over extracellular concentrations, with Zn^{2+} being shuttled to the deep store by the muffler. Recent experimental evidence suggests that the large-capacity deep store could be represented, in part or combination, by mitochondria (53), the endoplasmic reticulum/Golgi (17), and other sites of Zn^{2+} compartmentalization within the soma of cultured neurons (10).

The model provides an estimate of the resting intracellular free Zn^{2+} concentration in the soma of cultured cortical neurons. Given the constraint that, on average, 16% of ZnAF-2F is bound at rest, the resting intracellular free Zn^{2+} concentration in the presence of ZnAF-2F is 1.05 nM. When ZnAF-2F is removed from the model, this value increases slightly to 1.07 nM. It is interesting to note that this concentration of free Zn^{2+} represents ~500 free Zn^{2+} ions in the soma of a typically sized cortical neuron. This estimate is somewhat higher than the estimate obtained for HT-29 cells (38), and 100-fold higher than that obtained with PC-12 cells. Each study used a different method of estimating intracellular free Zn^{2+}, which could account for some of the differences; however, it is quite likely that different cell types and culture conditions result in different buffer capacity and set points for intracellular free Zn^{2+} levels.

The variability in resting ZnAF-2F saturation levels (i.e., differences in resting intracellular free Zn^{2+}) found in the experiments was attributed by the model to different levels of total Zn^{2+} in the cultured neurons. We did not systematically measure total Zn^{2+} and resting intracellular free Zn^{2+} in a series of different neuron cultures. However, it seems reasonable to expect that different cultures might vary in total Zn^{2+} content. What factors might cause such a variation? We would expect that the free and total Zn^{2+} concentrations of NB media remain within tight limits. Thus it is most likely that one or more intrinsic factors, beyond the control of the experimenter, determine the average Zn^{2+} content of particular cultures. For example, small changes in the culture density might lead to significant, albeit subtle, differences in expression of various genes influencing Zn^{2+} homeostasis. Even though the total Zn^{2+} content of resting cultured neurons seemed to vary, the neurons maintain resting intracellular free Zn^{2+} concentration within narrow limits. The model predicts that neurons accomplish this feat by increasing or decreasing the cellular muffler concentration to match the cellular Zn^{2+} load.

Neuronal free Zn^{2+} concentration is quite low and strongly buffered. The Zn^{2+} buffer capacity of neurons can be quantified using the method developed for estimating proton buffering capacity of cells (51). These authors defined buffer capacity as all of the cellular processes (including sequestration in cytoplasmic organelles, but excluding plasma membrane transport) that act to mitigate changes in cytosolic pH when cells are challenged with an acid or base load. A similar definition can be used to quantify Zn^{2+} buffer capacity and will allow the comparison of intrinsic buffer capacity in different cell types and provide a quantitative measure of changes in buffer capacity after physiological or pathological perturbations. Thus

$$\beta_{Zn} = \frac{d[Zn]}{dpZn} \quad (3)$$

where β_{Zn} is the intrinsic buffer capacity for Zn^{2+}, and d[Zn] and dpZn represent corresponding changes in the total cellular Zn^{2+} content (μM) and the −log of the intracellular free Zn^{2+} concentration, respectively. Using $^{65}Zn^{2+}$ uptake and model estimates of changes in intracellular free Zn^{2+} when cultured cortical neurons were exposed to 30 μM Zn^{2+}, we found that neuronal Zn^{2+} content changed 88 μM/min, whereas dpZn only changed 0.22 unit/min. Therefore, β_{Zn} for cultured cortical neurons is 396 μM/pZn unit. As eukaryotic cells evolved, Zn^{2+} and Ca^{2+} became important intracellular metals utilized in a host of biologically significant interactions because of availability and lack of redox activity. However, for both metals, even small increases in intracellular concentrations can be cytotoxic. Thus multiple protective mechanisms evolved to maintain free metal concentrations within narrow limits, one of these being cytosolic buffering through the use of soluble cytosolic metal binding proteins. In the case of Ca^{2+} buffering, a large family of EF-hand containing proteins shares responsibility for the control of resting cytosolic Ca^{2+} concentration and functions as Ca^{2+} sensors (4). The same may be true of cytosolic Zn^{2+} buffering. The large Zn^{2+} buffering capacity of neurons can be a "double-edged" sword. On the one hand, Zn^{2+} buffering capacity protects neurons from large swings in intracellular free Zn^{2+} concentrations, but on the other hand poses significant risk to the neuron when exposed to large

extracellular Zn^{2+} concentrations for prolonged periods. Under these conditions, large Zn^{2+} loads can be accumulated, and, since intracellular free Zn^{2+} remains low, efflux mechanisms at the plasma membrane are slow to eliminate such loads.

Role of MT in cytosolic Zn^{2+} buffering. We first explored whether MT could play a role in Zn^{2+} homeostasis as a simple Zn^{2+} buffer. Even when added at a concentration of 1 μM to *model 2*, which is greater than the 0.34 μM measured experimentally, MT could not buffer the Zn^{2+} loads described here. At rest, MT Zn^{2+} binding *sites 1-6* were nearly saturated, and *site 7* was largely free, and there was little change during exposure to 30 μM extracellular Zn^{2+}. For MT to be an effective cytosolic buffer in cultured neurons under the conditions of *model 2*, the concentration chosen for MT would have to be very much larger. However, MT certainly could play a more prominent role in simple cytosolic Zn^{2+} buffering in cell types other than cultured neurons, as has been shown in mouse lung fibroblasts (54).

In the MT as muffler model (*model 3*), we assumed that MT was exclusively responsible for sequestration of Zn^{2+} to the deep store. However, for MT to be an effective muffler of the Zn^{2+} loads applied in these studies, its concentration could not be small. Concentrations of 0.15, 0.5, or 1.0 μM could not shuttle enough Zn^{2+} to the deep store fast enough to match experimental constraints, but 2.0 μM could. If MT concentration is indeed low, then a more parsimonious explanation for MT's role in resting neurons is that MT is part of the high-affinity muffler pool represented in the muffler model (*model 2*). Interestingly, the low-affinity MT Zn^{2+} binding site, *site 7* (K_d of 20 nM), was able to shuttle Zn^{2+} to the deep store, at least as effectively as *site 6* (K_d of 100 pM) and more effectively than *site 5* (K_d of 40 pM) in these simulations, despite having much less Zn^{2+} bound at rest. Thus it may be more important to consider the relative Zn^{2+} binding site occupancy, particularly at *sites 6* and *7*, than the ratio of MT/T when considering the potential actions of MT as a muffler. On the other hand, the model predictions would be consistent with MT playing an important role in a neuron's long-term response to increased Zn^{2+} loads. In this situation, increases in MT protein expression (resulting in increased cellular concentrations) could allow MT to become the dominant cytosolic Zn^{2+} muffler. There are numerous examples and many treatments that have been shown to increase cellular MT levels severalfold (36). In addition, direct evidence of increased cytosolic Zn^{2+} buffering capacity with increased MT expression has been reported (38, 42).

MT may actually play a far more important role as a Zn^{2+} chaperone involved in pathways of Zn^{2+} trafficking, where MT transfers Zn^{2+} to highly specific cellular moieties (e.g., glutathione) under the control of cellular redox state (31, 32) or to mitochondrial transporters (11). For example, glutathione could facilitate the net movement of Zn^{2+} from MT to a deep store organelle or apoenzyme. We have included a transfer agent in models, but we have not reported the results here, because results were similar to those of the MT as muffler model (*model 3*) for parameter values chosen; also, there was no satisfying way to constrain the additional free parameters in the model for the transfer agent, especially since there are likely to be several different types of transfer agents with different concentrations and interaction rates with MT Zn^{2+} binding sites. Very little useful experimental data exist right now to inform such a model.

Routes for Zn^{2+} influx and efflux. The model uses a straightforward Michaelis-Menten description of Zn^{2+} influx. It is recognized that numerous studies have indicated that multiple pathways may exist for both the influx and efflux of Zn^{2+} in neurons (8). However, modeling influx in this way with efflux as a simple reversal of the influx process was adequate to match the experimental data. Concerning Zn^{2+} efflux, both experimental data and the model showed that efflux was small, even after neurons were maximally loaded with Zn^{2+} by exposure to ionophores, presumably a result of the large Zn^{2+} buffering capacity of neurons. In other words, even after a large Zn^{2+} load, intracellular free Zn^{2+} levels remain low and apparently are not enough to drive substantial amounts of Zn^{2+} efflux. No evidence for the active extrusion of Zn^{2+} (like that seen for Ca^{2+}) has been described to date. These data might appear to be in conflict with a previous report (20), but these experiments incubated neurons with Ca-EDTA for 1 h. Our experiments show a slow and steady Zn^{2+} efflux, which, after 1 h, would be expected to result in significant net Zn^{2+} release. Experimental evidence suggests that, when neurons are exposed to $^{65}Zn^{2+}$, a large portion (nearly 40% of the original load) of the accumulated tracer is surface bound. This may seem like a large amount, but there are many sites, including the glass surface on which the neurons are grown, that could provide ample Zn^{2+} binding sites. The model has yet to be expanded to include a description of channel-mediated Zn^{2+} influx and efflux (52), but this is a logical next step in the model development.

Insights into the cellular mechanisms of action of CQ. The model results indicate that the actions of CQ seen in the experiments are consistent with CQ acting primarily as a Zn^{2+} ionophore when added to cultured cortical neurons. At the concentrations of CQ added, CQ certainly did not significantly affect Zn^{2+} buffering capacity, as has been suggested by some to explain its mechanism of action in Alzheimer's disease. In the model, CQ binds to extracellular Zn^{2+}, crosses the plasma membrane, releases Zn^{2+} inside the neuron, and then returns to the extracellular space to rebind to Zn^{2+}. Both Zn^{2+} bound and free CQ cross the neuron membrane, according to their concentration gradients. Modeling the actions of CQ in this way was sufficient to reproduce the experimental results.

The addition of micromolar concentrations of CQ to cultured cells has been shown to have several important biological actions related to its presumed metal chelating activity when administered in vivo. For example, incubation with CQ and Zn^{2+} or Cu^{2+} for extended periods (6 h) resulted in large increases in cellular levels of Zn^{2+} or Cu^{2+} (61) and was responsible for an upregulation of metalloproteinase activity that caused a reduction in the production and secretion of Aβ 1-40 and 1-42. Other studies have shown that micromolar CQ can increase functional levels of hypoxia-inducible factor-1α, (protective in ischemic diseases) (5), and micromolar CQ downregulates mutant Huntington protein expression (46). Each of these effects could be due, at least in part, to the ionophoric actions of CQ shown here. Earlier studies have shown that much higher concentrations of CQ (1 mM) mediate cellular Cu^{2+} uptake (60). In the present report, CQ levels as low as 300 nM had discernible effects on the intracellular free Zn^{2+} concentration. Thus micromolar concentrations of CQ should be effective at increasing the total and intracellular free Zn^{2+} concentration in neurons, but require micromolar Zn^{2+}

concentrations to be present extracellularly. It should be noted that resting extracellular free Zn^{2+} in the brain is estimated to be <25 nM (19). This concentration is much too low to activate the ionophoric actions of CQ. Thus CQ would not be expected to be a generalized Zn^{2+} ionophore in the central nervous system. However, since extracellular Zn^{2+} levels during normal activity at Zn^{2+} containing glutamatergic synapses should be much greater (19), this mechanism provides for a selective synaptic effect in those neurons. The effective treatment dosage in humans is 250–750 mg daily, giving blood levels of ~10 μM (50). CQ shows a rapid brain uptake upon administration (47), but it is not known whether brain concentrations reach micromolar levels. Further studies will be required to determine the role that the ionophoric actions of CQ play in its various biological and therapeutic actions.

GRANTS

This work was supported by the Interdisciplinary Graduate Program in Molecular and Cellular Biology, Ohio University, and R. A. Colvin was supported by National Institute on Aging Grant AG20536.

REFERENCES

1. **Adamczyk M, Poznanski J, Kopera E, Bal W.** A zinc-finger like metal binding site in the nucleosome. *FEBS Lett* 581: 1409–1416, 2007.
2. **Bozym RA, Thompson RB, Stoddard AK, Fierke CA.** Measuring picomolar intracellular exchangeable zinc in PC-12 cells using a ratiometric fluorescence biosensor. *ACS Chem Biol* 1: 103–111, 2006.
3. **Canzoniero LMT, Turetsky DM, Choi DW.** Measurement of intracellular free zinc concentrations accompanying zinc-induced neuronal death. *J Neurosci* 19: 1–6, 1999.
4. **Case RM, Eisner D, Gurney A, Jones O, Muallem S, Verkhratsky A.** Evolution of calcium homeostasis: from birth of the first cell to an omnipresent signaling system: calcium channels and transporters. *Cell Calcium* 42: 345–350, 2007.
5. **Choi SM, Choi KO, Park YK, Cho H, Yang EG, Park H.** Clioquinol, a Cu(II)/Zn(II) chelator, inhibits both ubiquitination and asparagine hydroxylation of hypoxia-inducible factor-1 alpha, leading to expression of vascular endothelial growth factor and erythropoietin in normoxic cells. *J Biol Chem* 281: 34056–34063, 2006.
6. **Colvin RA.** pH dependence and compartmentalization of zinc transported across plasma membrane of rat cortical neurons. *Am J Physiol Cell Physiol* 282: C317–C329, 2002.
7. **Colvin RA, Davis N, Nipper RW, Carter PA.** Zinc transport in the brain: routes of zinc influx and efflux in neurons. *J Nutr* 130: 1484S–1487S, 2000.
8. **Colvin RA, Fontaine CP, Laskowski M, Thomas D.** Zn^{2+} transporters and Zn^{2+} homeostasis in neurons. *Eur J Pharmacol* 479: 171–185, 2003.
9. **Colvin RA, Fontaine CP, Thomas D, Hirano T, Nagano T, Kikuchi K.** Evidence for pH dependent Zn^{2+} influx in K562 erythroleukemia cells: studies using ZnAF-2F fluorescence and $^{65}Zn^{2+}$ uptake. *Arch Biochem Biophys* 442: 222–228, 2005.
10. **Colvin RA, Laskowski M, Fontaine CP.** Zinquin identifies subcellular compartmentalization of zinc in cortical neurons. Relation to the trafficking of zinc and the mitochondrial compartment. *Brain Res* 1085: 1–10, 2006.
11. **Costello LC, Guan Z, Franklin RB, Feng P.** Metallothionein can function as a chaperone for zinc uptake transport into prostate and liver mitochondria. *J Inorg Biochem* 98: 664–666, 2004.
12. **Dineley KE, Malaiyandi LM, Reynolds IJ.** A reevaluation of neuronal zinc measurements: artifacts associated with high intracellular dye concentration. *Mol Pharmacol* 62: 618–627, 2002.
13. **Ding WQ, Liu B, Vaught JL, Yamauchi H, Lind SE.** Anticancer activity of the antibiotic clioquinol. *Cancer Res* 65: 3389–3395, 2005.
14. **Eaton DL, Cherian MG.** Determination of metallothionein in tissues by cadmium-hemoglobin affinity assay. *Methods Enzymol* 205: 83–88, 1991.
15. **Eide DJ.** Zinc transporters and the cellular trafficking of zinc. *Biochim Biophys Acta* 1763: 711–722, 2006.
16. **Ellis CD, Wang F, MacDiarmid CW, Clark S, Lyons T, Eide DJ.** Zinc and the Msc2 zinc transporter protein are required for endoplasmic reticulum function. *J Cell Biol* 166: 325–335, 2004.
17. **Ellis CD, MacDiarmid CW, Eide DJ.** Heteromeric protein complexes mediate zinc transport into the secretory pathway of eukaryotic cells. *J Biol Chem* 280: 28811–28818, 2005.
18. **Ferrada E, Arancibia V, Loeb B, Norambuena E, Olea-Azar C, Huidobro-Toro JP.** Stoichiometry and conditional stability constants of Cu(II) or Zn(II) clioquinol complexes; implications for Alzheimer's and Huntington's disease therapy. *Neurotoxicology* 28: 445–449, 2007.
19. **Frederickson CJ, Giblin LJ, Krezel A, McAdoo DJ, Muelle RN, Zeng Y, Balaji RV, Masalha R, Thompson RB, Fierke CA, Sarvey JM, de Valdenebro M, Prough DS, Zornow MH.** Concentrations of extracellular free zinc (pZn)e in the central nervous system during simple anesthetization, ischemia and reperfusion. *Exp Neurol* 198: 285–293, 2006.
20. **Frederickson CJ, Suh SW, Koh JY, Cha YK, Thompson RB, LaBuda CJ, Balaji RV, Cuajungco MP.** Depletion of intracellular zinc from neurons by use of an extracellular chelator in vivo and in vitro. *J Histochem Cytochem* 50: 1659–1662, 2002.
21. **Frederickson CJ, Koh JY, Bush AI.** The neurobiology of zinc in health and disease. *Nat Rev Neurosci* 6: 449–462, 2005.
22. **Gaither LA, Eide DJ.** Functional expression of the human hZIP2 zinc transporter. *J Biol Chem* 275: 5560–5564, 2000.
23. **Gaither LA, Eide DJ.** The human ZIP1 transporter mediates zinc uptake in human K562 erythroleukemia cells. *J Biol Chem* 276: 22258–22264, 2001.
24. **Gaither LA, Eide DJ.** Eukaryotic zinc transporters and their regulation. *Biometals* 14: 251–270, 2001.
25. **Grynkiewicz G, Poenie M, Tsien RY.** A new generation of Ca^{2+} indicators with greatly improved fluorescence properties. *J Biol Chem* 260: 3440–3450, 1985.
26. **Gunzel D, Zimmermann F, Durry S, Schlue WR.** Apparent intracellular Mg^{2+} buffering in neurons of the leech Hirudo medicinalis. *Biophys J* 80: 1298–1310, 2001.
27. **Hidalgo J, Garcia A, Oliva AM, Giralt M, Gasull T, Gonzalez B, Milnerowicz H, Wood A, Bremner I.** Effect of zinc, copper and glucocorticoids on metallothionein levels of cultured neurons and astrocytes from rat brain. *Chem Biol Interact* 93: 197–219, 1994.
28. **Hirano T, Kikuchi K, Urano Y, Nagano T.** Improvement and biological applications of fluorescent probes for zinc, ZnAFs. *J Am Chem Soc* 124: 6555–6562, 2002.
29. **Hoops S, Sahle S, Gauges R, Lee C, Pahle J, Simus N, Singhal M, Xu L, Mendes P, Kummer U.** COPASI–a COmplex PAthway SImulator. *Bioinformatics* 22: 3067–3074, 2006.
30. **Huang L, Kirschke CP, Zhang Y, Yu YY.** The ZIP7 gene (Slc39a7) encodes a zinc transporter involved in zinc homeostasis of the golgi apparatus. *J Biol Chem* 280: 15456–15463, 2005.
31. **Jacob C, Maret W, Vallee BL.** Control of zinc transfer between thionein, metallothionein, and zinc proteins. *Proc Natl Acad Sci USA* 95: 3489–3494, 1998.
32. **Jiang LJ, Maret W, Vallee BL.** The glutathione redox couple modulates zinc transfer from metallothionein to zinc-depleted sorbitol dehydrogenase. *Proc Natl Acad Sci USA* 95: 3483–3488, 1998.
33. **Jiang LJ, Vasak M, Vallee BL, Maret W.** Zinc transfer potentials of the alpha- and beta-clusters of metallothionein are affected by domain interactions in the whole molecule. *Proc Natl Acad Sci USA* 97: 2503–2508, 2000.
34. **Kim AH, Sheline CT, Tian M, Higashi T, McMahon RJ, Cousins RJ, Choi DW.** L-type Ca^{2+} channel-mediated Zn^{2+} toxicity and modulation by ZnT-1 in PC12 cells. *Brain Res* 886: 99–107, 2000.
35. **Kirschke CP, Huang L.** ZnT7, a novel mammalian transporter, accumulates zinc in the golgi apparatus. *J Biol Chem* 278: 4096–4102, 2003.
36. **Klaassen CD, Liu J.** Induction of metallothionein in primary rat hepatocyte cultures. *Methods Enzymol* 205: 567–574, 1991.
37. **Krezel A, Hao Q, Maret W.** The zinc/thiolate redox biochemistry of metallothionein and the control of zinc ion fluctuations in cell signaling. *Arch Biochem Biophys* 463: 188–200, 2007.
38. **Krezel A, Maret W.** Zinc-buffering capacity of a eukaryotic cell at physiological pZn. *J Biol Inorg Chem* 11: 1049–1062, 2006.
39. **Krezel A, Maret W.** Dual nanomolar and picomolar Zn(II) binding properties of metallothionein. *J Am Chem Soc* 129: 10911–10921, 2007.
40. **Krezel A, Wojcik J, Maciejczyk M, Bal W.** May GSH and L-His contribute to intracellular binding of zinc? Thermodynamic and solution structural study of a ternary complex. *Chem Commun (Camb)* 6: 704–705, 2003.

41. **Lin W, Mohandas B, Fontaine CP, Colvin RA.** Release of intracellular Zn(2+) in cultured neurons after brief exposure to low concentrations of exogenous nitric oxide. *Biometals* 20: 891–901, 2007.
42. **Malaiyandi LM, Dineley KE, Reynolds IJ.** Divergent consequences arise from metallothionein overexpression in astrocytes: zinc buffering and oxidant-induced zinc release. *Glia* 45: 346–353, 2004.
43. **Malaiyandi LM, Vergun O, Dineley KE, Reynolds IJ.** Direct visualization of mitochondrial zinc accumulation reveals uniporter-dependent and -independent transport mechanisms. *J Neurochem* 93: 1242–1250, 2005.
44. **Mendes P.** Biochemistry by numbers: simulation of biochemical pathways with Gepasi 3. *Trends Biochem Sci* 22: 361–363, 1997.
45. **Neher E.** The use of fura-2 for estimating Ca buffers and Ca fluxes. *Neuropharmacology* 34: 1423–1442, 1995.
46. **Nguyen T, Hamby A, Massa SM.** Clioquinol down-regulates mutant Huntington expression in vitro and mitigates pathology in a Huntington's disease mouse model. *Proc Natl Acad Sci USA* 102: 11840–11845, 2005.
47. **Opazo C, Luza S, Villemagne VL, Volitakis I, Rowe C, Barnham KJ, Strozyk D, Masters CL, Cherny RA, Bush AI.** Radioiodinated clioquinol as a biomarker for beta-amyloid: Zn^{2+} complexes in Alzheimer's disease. *Aging Cell* 5: 69–79, 2006.
48. **Palmiter RD, Cole TB, Quaife CJ, Findley SD.** ZnT-3, a putative transporter of zinc into synaptic vesicles. *Proc Natl Acad Sci USA* 93: 14934–14939, 1996.
49. **Palmiter RD, Findley SD.** Cloning and functional characterization of a mammalian zinc transporter that confers resistance to zinc. *EMBO J* 14: 639–649, 1995.
50. **Ritchie CW, Bush AI, Mackinnon A, Macfarlane S, Mastwyk M, MacGregor L, Kiers L, Cherny R, Li QX, Tammer A, Carrington D, Mavros C, Volitakis I, Xilinas M, Ames D, Davis S, Beyreuther K, Tanzi RE, Masters CL.** Metal-protein attenuation with iodochlorhydroxyquin (clioquinol) targeting Abeta amyloid deposition and toxicity in Alzheimer disease: a pilot phase 2 clinical trial. *Arch Neurol* 60: 1685–1691, 2003.
51. **Roos A, Boron WF.** Intracellular pH. *Physiol Rev* 61: 296–434, 1981.
52. **Sensi SL, Canzoniero LMT, Yu SP, Ying HS, Koh JY, Kerchner GA, Choi DW.** Measurement of intracellular free zinc in living cortical neurons: routes of entry. *J Neurosci* 17: 9554–9564, 1997.
53. **Sensi SL, Ton-That D, Sullivan PG, Jonas EA, Gee KR, Kaczmarek LK, Weiss JH.** Modulation of mitochondrial function by endogenous Zn^{2+} pools. *Proc Natl Acad Sci USA* 100: 6157–6162, 2003.
54. **St. Croix CM, Wasserloos KJ, Dineley KE, Reynolds IJ, Levitan ES, Pitt BR.** Nitric oxide-induced changes in intracellular zinc homeostasis are mediated by metallothionein/thionein. *Am J Physiol Lung Cell Mol Physiol* 282: L185–L192, 2002.
55. **Suzuki T, Ishihara K, Migaki H, Ishihara K, Nagao M, Yamaguchi-Iwai Y, Kambe T.** Two different zinc transport complexes of cation diffusion facilitator proteins localized in the secretory pathway operate to activate alkaline phosphatases in vertebrate cells. *J Biol Chem* 280: 30956–30962, 2005.
56. **Suzuki T, Ishihara K, Migaki H, Matsuura W, Kohda A, Okumura K, Nagao M, Yamaguchi-Iwai Y, Kambe T.** Zinc transporters, ZnT5 and ZnT7, are required for the activation of alkaline phosphatases, zinc-requiring enzymes that are glycosylphosphatidylinositol-anchored to the cytoplasmic membrane. *J Biol Chem* 280: 637–643, 2005.
57. **Takeda A.** Movement of zinc and its functional significance in the brain. *Brain Res Rev* 34: 137–148, 2000.
58. **Thomas RC, Coles JA, Deitmer JW.** Homeostatic muffling. *Nature* 350: 564, 1991.
59. **Thompson RB, Peterson D, Mahoney W, Cramer M, Maliwal BP, Suh SW, Frederickson C, Fierke C, Herman P.** Fluorescent zinc indicators for neurobiology. *J Neurosci Methods* 118: 63–75, 2002.
60. **Treiber C, Simons A, Strauss M, Hafner M, Cappai R, Bayer TA, Multhaup G.** Clioquinol mediates copper uptake and counteracts copper efflux activities of the amyloid precursor protein of Alzheimer's disease. *J Biol Chem* 279: 51958–51964, 2004.
61. **White AR, Du T, Laughton KM, Volitakis I, Sharples RA, Xilinas ME, Hoke DE, Holsinger RM, Evin G, Cherny RA, Hill AF, Barnham KJ, Li QX, Bush AI, Masters CL.** Degradation of the Alzheimer disease amyloid beta-peptide by metal-dependent up-regulation of metalloprotease activity. *J Biol Chem* 281: 17670–17680, 2006.

J|A|C|S
COMMUNICATIONS

Published on Web 12/23/2007

Paramagnetic Relaxation-Based ^{19}F MRI Probe To Detect Protease Activity

Shin Mizukami,[†] Rika Takikawa,[†] Fuminori Sugihara,[‡] Yuichiro Hori,[†] Hidehito Tochio,[§] Markus Wälchli,[⊥] Masahiro Shirakawa,*[,§,¶] and Kazuya Kikuchi*[,†]

Division of Advanced Science and Biotechnology, Graduate School of Engineering, Osaka University, Osaka 565-0871, Japan, International Graduate School of Arts and Sciences, Yokohama City University, Kanagawa 230-0045, Japan, Department of Molecular Engineering, Graduate School of Engineering, Kyoto University, Kyoto 615-8510, Japan, Bruker BioSpin K.K., Ibaraki 305-0051, Japan, and CREST, Japan Science and Technology Corporation, Saitama 332-0012, Japan

Received September 12, 2007; E-mail: kkikuchi@mls.eng.osaka-u.ac.jp; shirakawa@moleng.kyoto-u.ac.jp

Real-time imaging of enzyme activities in vivo offers valuable information in understanding living systems and in developing medicine for various types of diseases. Currently, a variety of fluorescent probes for detecting enzyme activities are generally used for their high-sensitivity characteristics. However, general fluorescence imaging methods are not suitable for in vivo studies because visible fluorescence scarcely transmits through animal bodies. Although near-infrared fluorophores are useful for in vivo imaging for tissue surfaces, they cannot be applied to the deep section of the organ. On the other hand, magnetic resonance imaging (MRI) is known as an imaging technique adequate for in vivo studies.

^1H is a highly NMR-sensitive nuclide and abundant in living bodies. Thus, ^1H MRI is used as a powerful diagnostic imaging technique for identifying many human pathologies or medical conditions. Paramagnetic contrast agents such as several types of Gd complexes are in clinical use for their abilities to enhance the signal intensity by shortening the longitudinal relaxation time (T_1) of water protons. Presently, many scientists are interested in modifying the structures of the contrast agents to be functional in molecular imaging of biomolecules.[1] MRI probes for pH,[2] metal ions,[3] enzyme activities,[4] and so on have been developed. However, ^1H MRI often suffers from interference or low contrast due to the background signals from intrinsic ^1H, which hamper interpretation of the resultant images. Therefore, non-proton MRI is currently drawing a fair amount of attention.

One of the most promising nuclides for MRI is ^{19}F.[5] This nuclide has a high gyromagnetic ratio (γ) of 40.05 MHz/T and a 100% natural isotopic abundance ratio. Thus, the NMR sensitivity of ^{19}F is 0.83 relative to ^1H. Conveniently, due to their close γ values, ^{19}F NMR can be measured with most ^1H NMR instruments by appropriately tuning the RF coils. In our bodies, ^{19}F atoms are concentrated in the form of solid salts mostly in bones and teeth. Thus, the transverse relaxation time (T_2) of the intrinsic ^{19}F is extremely shortened,[6] and the MRI signal is hardly detectable. When ^{19}F-containing compounds are treated in human or animals, only the extrinsic ^{19}F MRI signals can be monitored without interference from background signals. For these above reasons, functional probes for ^{19}F MRI are very attractive for in vivo molecular imaging.

Known ^{19}F MRI probes are roughly categorized into two groups; one is the group of ^{19}F-containing compounds which accumulate in specific sites. Higuchi and co-workers synthesized a ^{19}F-containing thioflavin derivative that accumulates in amyloid β (Aβ) aggregates and visualized Aβ plaques in living animals by ^{19}F MRI.[7]

Scheme 1. Design Principle of ^{19}F MRI Probe Detecting a Protease Activity

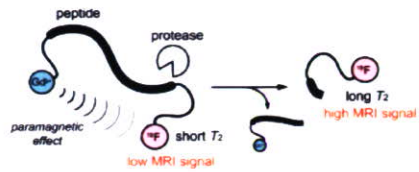

Another class of ^{19}F MRI probes is active agents.[5] They undergo chemical modification by the target molecules and then change their NMR parameters. Mason and co-workers have developed ^{19}F MRI probes detecting reporter enzyme activities by the chemical shift change.[8] These probes are hydrolyzed by the reporter enzyme and change the ^{19}F chemical shift. Although this approach is promising, this is highly dependent on the magnitude of chemical shift changes coupled with the target reaction, where sometimes the ranges of the chemical shift changes are limited. We here propose a novel design strategy for ^{19}F MRI probes in detecting protease activity.

We constructed a design principle whereby the intramolecular paramagnetic effect for T_2 of the ^{19}F NMR signal can be modulated by protease activities. T_2 is an important contrast factor for MRI, as the apparent intensity of the MRI signal directly depends on T_2 values. Generally, paramagnetic metal ions such as Fe^{3+}, Gd^{3+}, or the paramagnetic molecules such as O_2 shorten the T_2 of samples by paramagnetic relaxation enhancement (PRE).[9] In particular, Gd^{3+} has a very strong relaxivity (T_2-shortening activity) because of its large electron spin quantum number. When ^{19}F nuclei and a Gd^{3+} ion are attached to a short peptide, the ^{19}F nuclei exhibit a strong paramagnetic effect from the Gd^{3+}. Thus, the T_2 of the compound in the ^{19}F NMR would be shortened, and the MRI signal would be attenuated. If the peptide has a substrate sequence which can be cleaved by a certain protease, incubation of the compound with the protease should induce the extension of the T_2 and the enhancement of the ^{19}F MRI signal (Scheme 1).

According to the above strategy, we synthesized a ^{19}F MRI probe, Gd-DOTA-DEVD-Tfb, for detecting caspase-3 activity (Figure 1). Caspase-3 is a marker enzyme of apoptosis and is used in the evaluation of anticancer agents inducing apoptosis of tumor cells. The probe consists mainly of three parts, which are a Gd^{3+} complex, an enzyme substrate peptide, and a ^{19}F-containing group. The peptide sequence is DEVD because caspase-3 selectively cleaves the C-terminal peptide bond of the sequence DXXD (X: optional).[10] A macrocyclic metal ligand, DOTA, was attached via a β-alanine linker with the N-terminus of ^{19}F-containing peptide DEVD-Tfb, which was synthesized by Fmoc solid-phase peptide synthesis. The ligand-conjugated peptide, DOTA-DEVD-Tfb, was complexed with Gd^{3+} ion and purified with a reversed-phase HPLC to yield Gd-

[†] Osaka University.
[‡] Yokohama City University.
[§] Kyoto University.
[⊥] Bruker BioSpin K.K.
[¶] CREST, JST.

 10.1021/ja077058z CCC: $40.75

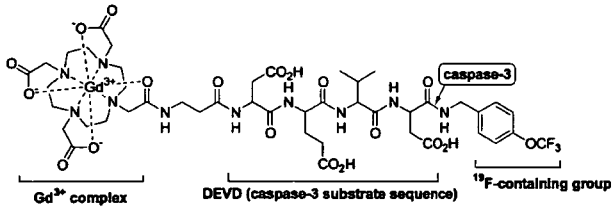

Figure 1. Structure of Gd-DOTA-DEVD-Tfb.

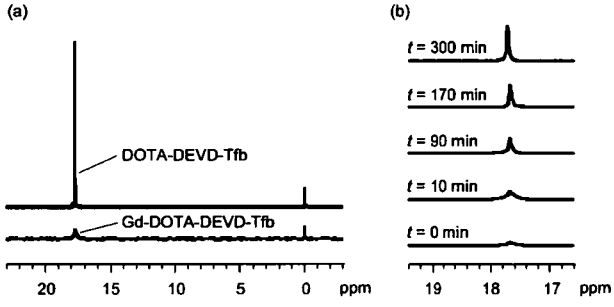

Figure 2. (a) ^{19}F NMR spectra of DOTA-DEVD-Tfb (1 mM) and Gd-DOTA-DEVD-Tfb (1 mM). Sodium trifluoroacetate was added as an internal standard (0 ppm). (b) Time-dependent ^{19}F NMR spectral change of Gd-DOTA-DEVD-Tfb with caspase-3 at 37 °C.

DOTA-DEVD-Tfb. The probe structure was identified with ESI-TOF MS, and its purity was confirmed by HPLC and ^{19}F NMR.

Next, we measured the ^{19}F T_1 and T_2 values of the probe free from and in complex with Gd^{3+}. The T_1 and T_2 of DOTA-DEVD-Tfb (1 mM) were 1.910 and 0.326 s, respectively. In contrast, the values of Gd-DOTA-DEVD-Tfb could not be measured, due to markedly shorter relaxation times and the low signal intensity of the ^{19}F resonance. This result indicates that the ^{19}F nucleus of Gd-DOTA-DEVD-Tfb undergoes strong PRE by Gd^{3+}. This effect was explicitly shown in the one-dimensional ^{19}F NMR spectrum, in which the peak intensity of Gd-DOTA-DEVD-Tfb was largely decreased with broadening as compared with that of DOTA-DEVD-Tfb (Figure 2a). When we treated the Gd-DOTA-DEVD-Tfb with caspase-3 at 37 °C, the ^{19}F NMR peak became sharper and higher in a time-dependent manner (Figure 2b). This indicated the intramolecular paramagnetic effect from Gd^{3+} to ^{19}F was cancelled by the cleavage of the probe. The T_1 and T_2 of the 1 mM cleaved product were extended to 0.122 and 0.032 s, respectively. These values are still shorter than those of DOTA-DEVD-Tfb. An additional experiment suggests that this is because of the intermolecular PRE by the Gd^{3+} complex (Figure S4 in Supporting Information).

Finally, an attempt was made to visualize caspase-3 activity using a ^{19}F MRI phantom to verify the practical applicability of this probe and its sensing principle. As was expected, Gd-DOTA-DEVD-Tfb showed no signal on the ^{19}F MRI phantom image. Time course of the density-weighted ^{19}F MR images of Gd-DOTA-DEVD-Tfb with and without caspase-3 are shown in Figure 3. Caspase-3 activity induced a noticeable signal enhancement. This result is compatible with the one-dimensional ^{19}F NMR data shown in Figure 2b. We used a relatively high probe concentration for MRI because of the sensitivity limitation due to our current instrument setup. However, the intrinsically high sensitivity for the ^{19}F signal of the probe is demonstrated by the NMR spectra measured at 1−5 μM by a well-tuned spectrometer (Figure S5 in Supporting Information). This result indicates the possibility that a suitable instrument enables in vivo ^{19}F MR imaging in the future.

In conclusion, a novel design principle of ^{19}F MRI probes detecting protease activity was developed. This principle is based

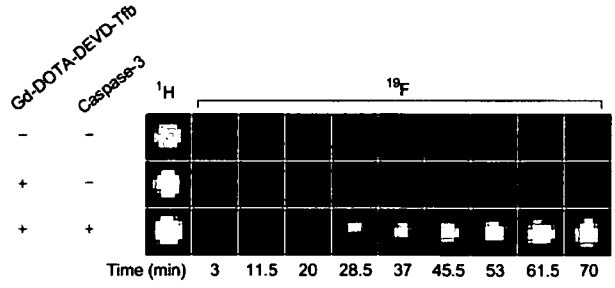

Figure 3. Time course of density-weighted ^{19}F MR images of Gd-DOTA-DEVD-Tfb (1 mM) with or without caspase-3 at 37 °C.

on MRI signal quenching from the intramolecular paramagnetic effect of Gd^{3+}. The intramolecular Gd^{3+} made the T_2 of the probe too short to be measured, with the paramagnetic effect which can be cancelled by the probe hydrolyzation by caspase-3. T_2 is a parameter that can be used to generate contrasts in MR images. Using this probe as a positive contrast agent, we demonstrated that the probe could detect caspase-3 activity spatially from the phantom image using ^{19}F MRI. This method could be applied to the sensing of not only other kinds of proteases but also other hydrolases such as nucleases and phosphodiesterases. It is expected that this sensing strategy might become the basis for the next stage of in vivo molecular imaging techniques.

Acknowledgment. This work was supported by MEXT of Japan, by JST, by the Mitsubishi Foundation, by Kato Memorial Bioscience Foundation, by Astellas Foundation for Research on Metabolic Disorders, by the Uehara Memorial Foundation, by Terumo Life Science Foundation, by Nagase Science and Technology Foundation and by the Asahi Glass Foundation to K.K., by the Cosmetology Research Foundation to S.M., by CREST (JST) to M.S. We thank Dr. Tetsuro Kokubo at Yokohama City University for the use of MRI instrument.

Supporting Information Available: Detailed experimental procedures and supplementary results. This material is available free of charge via the Internet at http://pubs.acs.org.

References

(1) (a) Jasanoff, A. *Trends Neurosci.* **2005**, *28*, 120−126. (b) Sosnovik, D. E.; Weissleder, R. *Curr. Opin. Biotechnol.* **2007**, *18*, 4−10.
(2) (a) Zhang, S.; Kuangcong, W.; Sherry, A. D. *Angew. Chem., Int. Ed.* **1999**, *38*, 3192−3194. (b) Aime, S.; Barge, A.; Castelli, D. D.; Fedeli, F.; Mortillaro, A.; Nielsen, F. U.; Terreno, E. *Magn. Reson. Med.* **2002**, *47*, 639−648.
(3) (a) Li, W.; Fraser, S. E.; Meade, T. J. *J. Am. Chem. Soc.* **1999**, *121*, 1413−1414. (b) Hanaoka, K.; Kikuchi, K.; Urano, Y.; Narazaki, M.; Yokawa, T.; Sakamoto, S.; Yamaguchi, K.; Nagano, T. *Chem. Biol.* **2002**, *9*, 1027−1032.
(4) (a) Louie, A. Y.; Hüber, M. M.; Ahrens, E. T.; Rothbächer, U.; Moats, R.; Jacobs, R. E.; Fraser, S. E.; Meade, T. J. *Nat. Biotechnol.* **2000**, *18*, 321−325. (b) Perez, J. M.; Josephson, L.; O'Loughlin, T.; Högemann: Weissleder, R. *Nat. Biotechnol.* **2002**, *20*, 816−820. (c) Yoo, B.; Pagel, M. D. *J. Am. Chem. Soc.* **2006**, *128*, 14032−14033. (d) Chen, J. W.; Sans, M. Q.; Bogdanov, A.; Weissleder, R. *Radiology* **2006**, *240*, 473−481.
(5) Yu, J.; Kodibagkar, V. D.; Cui, W.; Mason, R. P. *Curr. Med. Chem.* **2005**, *12*, 819−848.
(6) Code, R. F.; Harrison, J. E.; McNeill, K. G.; Szyjkowski, M. *Magn. Reson. Med.* **1990**, *13*, 358−369.
(7) Higuchi, M.; Iwata, N.; Matsuba, Y.; Sato, K.; Sasamoto, K.; Saido, T. C. *Nat. Neurosci.* **2005**, *8*, 527−533.
(8) (a) Cui, W.; Otten, P.; Li, Y.; Koeneman, K. S.; Yu, J.; Mason, R. P. *Magn. Reson. Med.* **2004**, *51*, 616−620. (b) Yu, J.; Liu, L.; Kodibagkar, V. D.; Cui, W.; Mason, R. P. *Bioorg. Med. Chem.* **2006**, *14*, 326−333.
(9) Helm, L. *Prog. Nucl. Magn. Reson. Spectrosc.* **2006**, *49*, 45−64.
(10) Thornberry, N. A.; Rano, T. A.; Peterson, E. P.; Rasper, D. M.; Timkey, T.; Garcia-Calvo, M.; Houtzager, V. M.; Nordstrom, P. A.; Roy, S.; Vaillancourt, J. P.; Chapman, K. T.; Nicholson, D. W. *J. Biol. Chem.* **1997**, *272*, 17907−17911.

JA077058Z

3-2 情報素子としてのシナプス
構造・機能ならびに新たな疾患制御標的としての意義

奥野浩行 東京大学大学院医学系研究科
藤井 哉 東京大学大学院医学系研究科
尾藤晴彦 東京大学大学院医学系研究科

1 はじめに

脳は，人間が人間たる所以の臓器である．脳の機能により，人間は社会活動を円滑に行い，文化的な生活を営むことができる．少子化と高齢化が急速に進行しつつある超成熟型社会の日本では，①脳の機能発達を助け，②脳高次機能を維持し続け，③脳高次機能低下を予防し，さらに，④一度障害された場合でも可能な限り再建する，というチャレンジが21世紀医療の中核課題の1つであることは間違いない．

最近の知見により，発育時における神経ネットワークの発達異常が，精神・認知活動などの機能的障害をもたらす根本原因の1つである，という考え方が有力視されている．また，正常な脳発達をとげた後でも，加齢とともに微小な神経回路の機能不良が徐々に蓄積し，ある閾値を超えると，意識，情動，記憶，意欲，注意などの脳高次機能に障害が発生するリスクが高くなる．神経ネットワークや局所神経回路を理解するためには，まず脳の情報処理の素過程を担い，神経回路のノードであるシナプスの基本的作動原理を解明することが重要である．

本稿では，このような視点からシナプスをとらえ，脳の基本情報素子の機能と構造について概説し，疾患制御標的としての意義について触れてみたい．

2 シナプスとは

シナプスの存在は，19世紀の脳神経科学者らにより予言されていた．たとえば，1906年にノーベル医学生理学賞を受賞したRamon y Cajalは，自身の提唱したニューロン説（neuron doctrine）において，「神経細胞（ニューロン）は互いに融合せず，接触している」と喝破しており，脳全体では1000億個以上ともいわれるニューロンが，互いの接触（＝シナプス）を介して情報交

換を行い，入力に対する出力をリアルタイムに制御していることを，解剖学的知見により鋭く洞察した．

神経幹細胞から生じたニューロンは，分裂後の分化・成熟にしたがい，細胞極性の形成と同時に，軸索ならびに樹状突起と呼ばれる2種類の機能的に分化した突起を伸ばす．軸索の先端の神経終末には，神経伝達物質放出を司る分子装置が整備され，一方の樹状突起上にはシナプス後肥厚部（postsynaptic density，PSD）と呼ばれる神経伝達物質を受け取り，細胞内へ情報を伝達する特殊な構造が作られ，これらが対をなして細胞間接着点であるシナプスを形成する．つまりシナプスとは，神経伝達物質の放出と受容を介して，情報をシナプス前細胞からシナプス後細胞へ伝達する装置である．ニューロンの成熟にともない，シナプスは1つのニューロンあたり，数百から数千個，多い場合では数万以上も形成される．すなわち1つのニューロンは，数百から数万にもおよぶ多数のほかのニューロンから情報を受け取っているのである．

シナプスが形成され，成熟な神経ネットワークが完成した後は，ニューロンの形態やシナプス結合は大きく変化せず，その構造を支える細胞骨格系は静的である，という考えが長らく主流であった．そのなかで，たとえばDonald Hebbは彼の著書“The organization of behavior”（1949）のシナプス可塑性に関する理論的考察の中で，シナプスの増減を説明しうる機構として，活動依存的な突起の動的な新生・消退をあげている．その後，半世紀以上経た現在，実際に，神経活動に伴いシナプスの形態の変化が起こることが，実験によって明らかにされつ

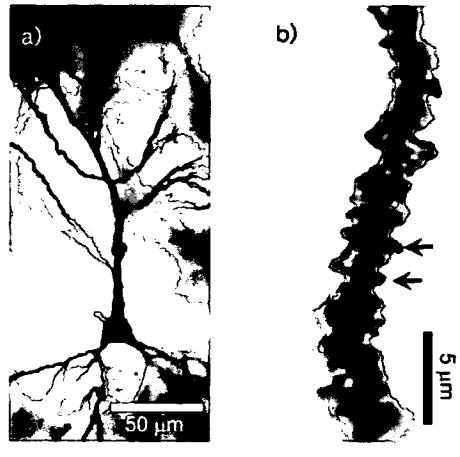

図3-2-1 神経細胞の形態
(a) ラット海馬の錐体細胞のゴルジ染色像．細胞体から1本の尖頭樹状突起（apical dendrite）および複数の基底樹状突起（basal dendrites）が伸びる様子が見られる
(b) 樹状突起の拡大写真．樹状突起に無数の棘＝スパイン（矢印）が存在する

つある．大脳皮質におけるもっとも主要な神経伝達物質は，グルタミン酸であるが，これを受け取る興奮性のシナプス後肥厚部の多くは，スパインと呼ばれる樹状突起上の微小な突起に形成されている（図3-2-1）．

最近，長期増強（LTP）や長期抑圧（LTD）などのシナプス伝達の可塑的変化に伴い，スパイン，スパイン頸部，スパイン数などが変化することが相次いで報告され，シナプスおよびニューロンの形態は，成熟脳においてもダイナミックに変化しているという共通概念が定着してきた[1]．発達期における軸索および樹状突起の形成・伸展やシナプス形成過程ならびに成熟期におけるシナプスの構造的変化には，アクチンや微小管などの細胞骨格の動的役割が不可欠と考えられている[2, 3]．

3 シナプス構造

それでは，シナプスの構造と特徴とはいかなるものであるか．

ニューロン間で刻一刻と伝達される神経情報は，前述のとおり，シナプス前膜では神経伝達物質放出として表現され，シナプス後膜においては，神経伝達物質が膜表面に存在する受容体に捕らえられた後，電気的シグナルと化学的な細胞内シグナルに振り分けられる．電気的シグナルおよび化学的細胞内シグナルは，隣接する，または離れた場所に存在する複数のシナプス間で加算・引算などの演算が行われ，その結果は出力として次のニューロンに伝えられていく．これらの素過程が並列的に脳内の神経回路内で起こり，その総和として，人間の精神・認知・神経活動が起こると考えられている．すなわち，脳高次機能と呼ばれる意識，情動，記憶，意欲，注意などの機能は，シナプス後膜の神経伝達物質受容体の構造変化に伴うイオン透過・膜電位変化と，分子シグナリング（酵素反応およびタンパク質-タンパク質間相互作用，タンパク質-脂質二重膜間相互作用や細胞骨格相互作用の総和）に還元できるといっても過言ではない．

ここで考慮に入れなければならないのが，この電気的および分子シグナリングの起こるフィールドの大きさである．興奮性シナプスが存在する樹状突起のスパインの容積は，1フェムトリットル以下である（図3-2-2）．このような局所空間では，通常の試験管内の反応とは異なり，反応に関与する分子の数が

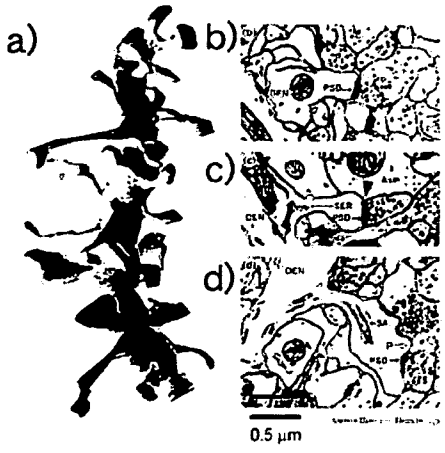

電子顕微鏡写真像から再構成した海馬錐体細胞の樹状突起スパインの体積:
0.004-0.56 μm^3 (=fL)

例えば体積0.16 μm^3のスパインに含まれる分子の数は、

濃度1 μMでは

1×10^{-6} (M) x 0.16 x 10^{-15} (L) x 6.02 x 10^{23} = 1 x 10^2 分子

濃度10 nMでは

10×10^{-9} (M) x 0.16 x 10^{-15} (L) x 6.02 x 10^{23} = 1 分子

である。

図3-2-2 海馬錐体細胞シナプスの微細構造

(a) 連続電子顕微鏡写真から再構成した樹状突起の三次元構造

(b～d) 個々の電子顕微鏡写真．前シナプス部位（20～40nmほどの小胞＝シナプス小胞が多数含まれる部位）や後シナプス部位（PSDを含む部位）が示されている（文献14より許可を得て転載）．電子顕微鏡写真による再構成から計算されたスパインの体積は，かなり幅のある分布を示す．この極微小体積においては，シナプスタンパク質などの分子は数分子～数百分子程度の数にしかならない

非常に少ないため，効率よく化学反応を起こすための特殊な機構が存在すると考えられている[4]．すなわち，自由拡散により酵素と基質が衝突するのではなく，数十nm四方の「ナノドメイン」に濃縮された関連分子の間で，効率よくシグナルが共役・伝達されていると考えられる．詳しくは後に述べるが，実際，シナプス後肥厚部にはシグナル伝達に関わる分子が高密度に存在している．このようなナノドメイン内における代謝反応論・酵素学の実体は，これまでほとんど明らかにされていない．

一方，樹状突起スパインの構造に柔軟性があることは前項で述べたが，このことは，少なくとも大脳皮質の興奮性伝達を担うシナプスにおいては，ナノドメインの大きさ自体が，神経ネットワークの活動自体によって変化する性質を有していることを示す．このナノドメインの変化は，そこに存在するシグナル伝達関連分子の組成のダイナミックな再編成を引き起こし，それに伴い，ナノドメインでの化学反応過程も大きく変化すると考えられる．

4 シナプスの発達と神経精神疾患

シナプスが精神・認知活動の素子であり，その形態・機能はダイナミックに変化しうるが，シナプスの形態と脳機能にはどのような関係が知られているのであろうか．大脳における興奮性シナプス構造の形成の場である樹状突起スパインは，脳の発達と共にその密度や形態が大きく変化する（図3-2-3 a）．胎児期においては，スパインは細長く，樹状突起の単位長さあたりの密度も低いが，生後，より短く太いスパインが増え，密度も飛躍的に高くなる．

このような形態の変化が脳機能の発達に重要であることは，精神遅滞や精神神経疾患において，顕著なシナプス構造の変化が数多く報告されていることからも強く示唆される（図3-2-3 b）．精神遅延症状を示す患者の大きな割合を占める脆弱性X症候群やダウン症候群では，スパイン密度の低下やスパイン形態が細長くなる，といった共通した所見が報告されている[5]．発育時におけるシナプスの発達異常が，精神・認知障害をもたらす根本原因の1つであるという考えに基づき，これら障害の克服のためにはシナプス形成とシナプス構造の安定性と動的変化を支配する，分子細胞生物学的基盤を明らかにする必要がある．

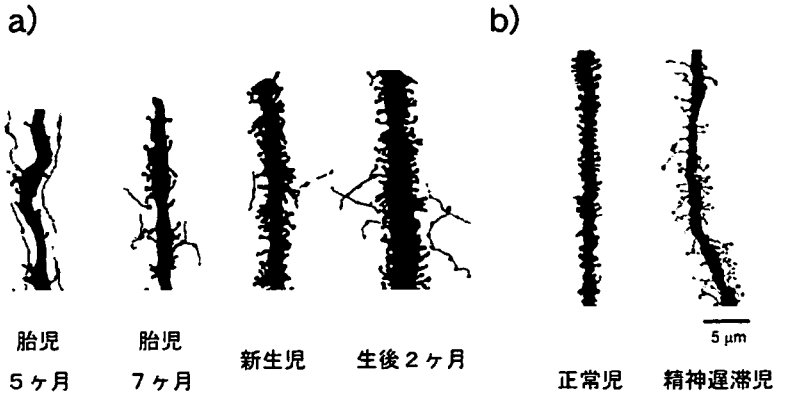

図3-2-3 樹状突起スパインの発達と形態異常

(a) 大脳の発達とスパインの形態変化．大脳新皮質錐体細胞のゴルジ染色像を示す．発達とともに樹状突起単位長さあたりのスパインの数が増加している（文献15より許可を得て転載）

(b) 正常児（6ヶ月）および精神遅滞児（10ヶ月）の大脳新皮質の錐体細胞のゴルジ染色像．精神遅延児の脳では，正常児脳と比べ，細長いスパインが数多く存在し，スパイン密度も低い（文献16より許可を得て転載）

5 シナプス伝達を担うシナプス後肥厚部分子複合体

シナプス前終末からの神経伝達放出は，軸索を伝わる活動電位が神経終末に到着してから1ミリ秒程度のきわめて短い時間内に，シナプス小胞（synaptic vesicles）がシナプス前膜へ膜融合することによって引き起こされる．このような，きわめて高い時間的信頼性をもつ神経伝達物質放出を保証するための，電位依存性カルシウムチャネル開口とシナプス小胞の間の距離が最適化されることや，小胞放出機構の高いカルシウム協調性が存在するなどの機構が明らかにされつつある[6]．

一方，シナプス後肥厚部におけるシグナルは，神経伝達物質受容体が伝達物質を結合し，構造変化を起こすことに始まる．NMDA型やAMPA型のグルタミン酸受容体のように，リガンド結合型イオンチャンネルを形成している場合，リガンド結合後，やはり1ミリ秒以内にチャネルのゲートが開き，イオン透過が起こり，数ミリ秒以内に電流が不活性化する．一方，mGluRのような代謝型受容体の場合は，三量体Gタンパク質の活性化によるシグナル増幅を介するため，シグナル伝達の活性化は秒のオーダーとなり，チャネル型受容体と比べてかなり遅れるが，複数の特異的な下流エフェクター分子の活性制御を行うことにより，多彩な細胞内シグナル伝達経路の平行制御が可能となる[4, 7]．

シナプス前部・後部にかかわらず，ナノドメインに濃縮されたシグナル伝達分子の間で協調的なシグナル伝達を再現性よく伝達し，同時にその制御を可能にする機構を実現しているのが足場タンパク質の存在である．多くの足場タンパク質は，多量体化する性質とマルチドメイン構造を併せ持ち，これにより限られた空間内で複雑な分子ネットワークが形成されている（図3-2-4）．この分子ネットワークにおいて，足場タンパク質は特異的なシグナリング分子との複合体を形成してシグナル伝達の場を提供し，シグナル伝達の特異性，正確性，そして感受性を制御すると考えられているが，その全体像はいまだ明らかではない．生きたニューロンのシナプス構造の中で，分子複合体の動態を実測し，同時に細胞内シグナル伝達の開始・持続・終了を測定することが技術的に困難だからである．筆者らは，この技術的困難のブレークスルーを見いだすことが，現在のナノ技術の向かうべき方向の1つであると考えている．

興奮性シナプスを形成するスパイン内には，アクチン細胞骨格（F-actin）

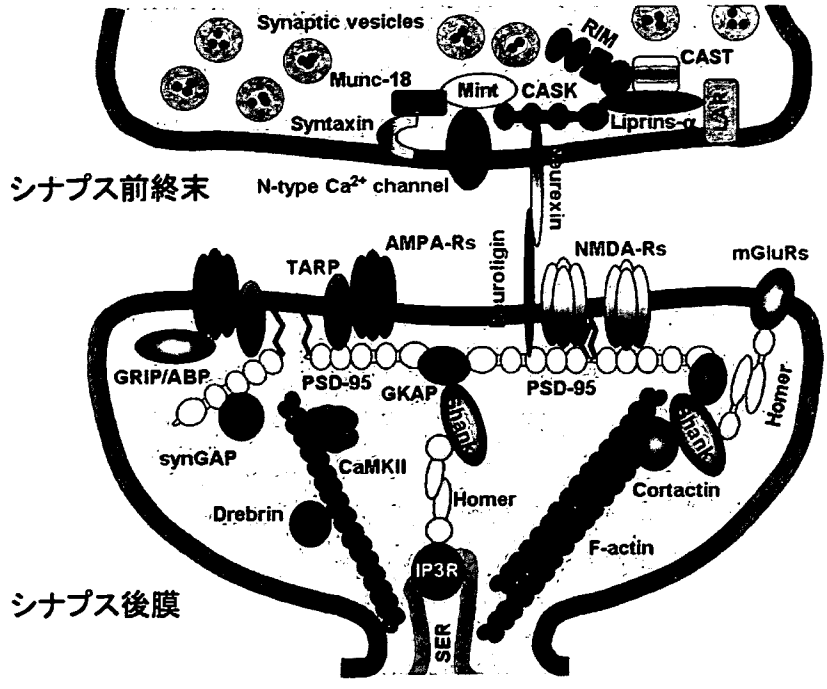

図3-2-4　興奮性シナプスの構成タンパク群

中枢神経の興奮性シナプスにおけるシナプス前終末，およびシナプス後膜に存在するタンパク質，およびそれらの相互作用のごく一部を模式的に示した．シナプス前終末では，活動電位によりシナプス小胞（synaptic vesicles）を膜に融合し，神経伝達物質を放出するために必要な複合体がタンパク相互作用により形成されている．また，シナプス後膜では興奮性シナプス伝達の主要な担い手である膜タンパク質AMPA型グルタミン酸受容体（AMPA-Rs）やNMDA型グルタミン酸受容体（NMDA-Rs），また，代謝型グルタミン酸受容体（mGluRs），およびそれらを支える細胞内の足場タンパク質（scaffolding proteins），さらに，それらに結合するさまざまなタンパク質が高密度で存在している

が高度に集積しており，アクチン分子の重合・脱重合を制御することにより，スパイン形態の動的な変化が制御されていると考えられている．実際，アクチン細胞骨格（F-actin）を調節する低分子量Gタンパク質Rhoファミリー GTPaseの関連分子であるCitronやCollibistin，Kalirinなどは，スパイン内に局在しており，これらが足場タンパク質に結合することにより分子ネットワークを構成していることが報告されている[8]．これらの分子の活性を神経活動依存的に制御する機構は現在のところ明らかになっていない．

シナプス後肥厚部における複雑な分子ネットワークは，アクチン細胞骨格とシナプス後肥厚部タンパク質の複合体によって形成されているが，シナプス後肥厚部タンパク質はアクチン重合阻害により動態が著しく影響を受ける成分